The Henryk Niewodniczański
INSTITUTE OF NUCLEAR PHYSICS
Polish Academy of Sciences
ul. Radzikowskiego 152, 31-342 Kraków, Poland

Raport No. 2051/AP

Test of the European Transport Solver in the frame of Integrated Tokamak Modelling

Dariusz Twaróg, Roman Stankiewicz[1], Krzysztof Drozdowicz

[1]Institute of Plasma Physics and Laser Microfusion, Warsaw, Poland

Abstract

The European Transport Solver (ETS) is developed in the frame of Project 3 of EFDA Integrated Tokamak Modeling Task Force. Several numerical methods are implemented in the ETS. This paper presents a method of verification of implemented numerical schemes for the case of solutions which take into account existence of the transport barrier in the tokamak plasma. A manufactured solution method for generation of exact solutions is developed for this case. The exact solutions are compared with the numerical ones for a simple transport model. Numerical tests demonstrate that numerical procedures: solvers 3 and 7 can reproduce analytic solutions with a discontinouity quite well.

1. Introduction

The Institute of Plasma Physics and Laser Microfusion (IPPLM), under Contract of Association between the EURATOM (the European Atomic Energy Community) and the IPPLM, coordinates the work on controlled thermonuclear fusion research carried on in Polish science centers. These works concern plasma physics and technology for Magnetic Confinement Fusion (MCF) toroidal thermonuclear devices (tokamaks and stellarators). These works included about twenty tasks provided by different research units. In the field of plasma diagnostics the Department of Radiation Transport Physics in the Institute of Nuclear Physics is involved in the development of diamond detectors to detect escaping fast alpha particles and other ions and also method of activative fissionable samples (utilizing the delayed neutron measurement). The department of Radiation Transport Physics (Laboratory 54) participates also in the Integrated Tokamak Modelling Task Force (ITM-TF) Project 3 for development of the European Transport Solver which is devoted to provide the complete simulation of the discharge in a tokamak like ITER including the core, the edge and the scrap-off layer.

2. Physics

Fusion energy research began in early 1950s and was developed in two main paths: inertial confinement fusion and magnetic confinement fusion. By the mid fifties, Lawson identified the product of plasma density and of energy confinement time, $n\tau_E$, as a critical parameter for the thermonuclear reactor [1]. Power balance in his analysis showed that fuel density, n, and plasma energy confinement time, τ_E, was a function of plasma temperature, T. For parabolic density and temperature profiles the ignition requirement on the peak value is:

$$\hat{n}\hat{T}\tau_E > 5\times10^{21}\ \mathrm{keV\cdot s\cdot m^{-3}}, \tag{1}$$

where $\hat{n}$ and $\hat{T}$ are the peak of ions density and temperature in the plasma and τ_E is the energy confinement time.
A measure of the success in approaching reactor condition is given by the ratio Q, of the thermonuclear power produce P_{TNP} to the heating power P_H supplied, that is:

$$Q = \frac{P_{TNP}}{P_H} \tag{2}$$

In the case of commercial thermonuclear power plant Q has to be bigger then 15. At ignition, where P_H is reduced to zero where no external heating is required, $Q \to \infty$ [2].
Since the early 1950s forward, there have been two major approaches to fusion energy: internal confinement fusion and magnetic confinement fusion. In the magnetic confinement fusion approach, a magnetic bottle is formed which confines hot plasma for a long periods of time approaching steady-state conditions. Nowadays, after almost sixty years of study, stellarators and tokamaks seem to be the most promising devices for plasma confinement in toroidal configuration.

The tokamak is a toroidal plasma confinement system where plasma is confined by a magnetic field. The principal field is the toroidal field B_t but it alone is unable to confine plasma. In order to have an equilibrium in which the plasma pressure is balanced by the magnetic forces it is necessary to have additionally a poloidal magnetic field B_p. In a tokamak this field is produced mainly by the current I_p flowing in the toroidal direction [2]. A combination of the toroidal and poloidal fields gives rise to magnetic field lines which have a helical trajectory around the torus as shown in Fig. 1. In a stellarator the poloidal field is supplied by external coils [3]. The tokamaks rely on a toroidal plasma current for the generation of the poloidal field. Generally, the toroidal current I_p in a tokamak is generated inductively by means of a transformer, in which plasma acts as a secondary winding coil. This immediately leads to major limitations of tokamak operation: the finite flux swing of the transformer in a combination with the finite resistivity of plasma results in a finite pulse length during which plasma is contained inside tokamak. This has motivated a development of alternative ways for the generation of the toroidal plasma current I_p. Neoclassical, collisional transport [4] in a high pressure toroidal plasma (*H-mode*) together with gradient of the toroidal magnetic field B_t generates a finite parallel plasma current flowing in poloidal direction. This current is known as the bootstrap current and is entirely self generated by the plasma [5]. As we can foresee now, the fully non-inductive, steady state operation of ITER and future tokamak fusion reactors will have to rely on the bootstrap current for supplying the major part of the plasma current.
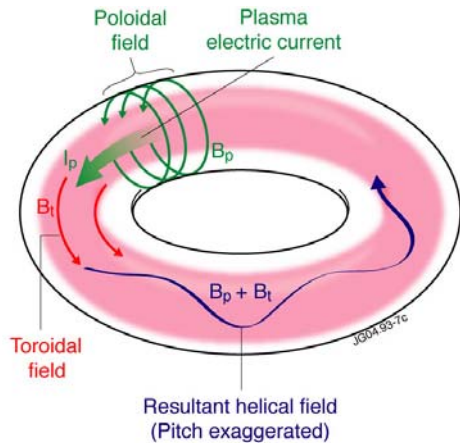

Fig. 1. Toroidal magnetic field B_t and poloidal magnetic field B_p due to toroidal current I_p [6].
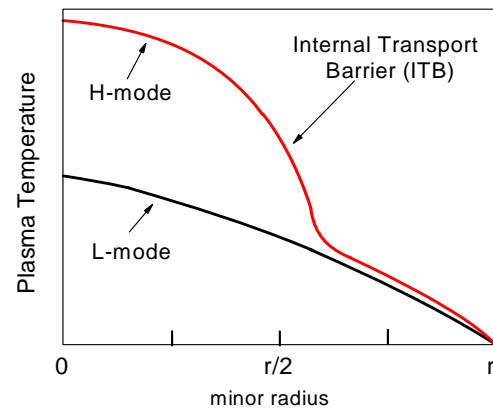
Fig. 2. Tokamak temperature profiles for H-mode (red curve) and for L-mode (black curve).

The *H-mode* ("high" confinement mode) has been first time observed in tokamak ASDEX [7]. It is characterized by an improvement of the energy confinement time by a factor two compared to the standard *L-mode,* these modes are illustrated in Fig. 2. Detailed physics studies of the *H-mode* over next decades helped to provide a fundamental understanding of plasma behavior in a tokamak. Transport of energy and particles in tokamak plasma is mostly caused by turbulence originated from micro-instabilities. Under certain conditions these instabilities together with stabilizing effect of the Magnetohydrodynamics (MHD) lead to internal transport barriers (ITBs) formation, an area characterized by steep gradients of plasma profiles in the core (Fig. 2) [8]. Now thirty years later, the *H-mode* with a solid experimental base is very robust and has been chosen as the baseline operating mode for

ITER [9]. Therefore robust and accurate methods of modeling of the plasma transport barrier dynamics are essential for understanding the tokamak behavior. Predictive modeling of plasma transport requires a good physical model of plasma transport as well as a good numerical procedure that would be able to cope with strong nonlinearity of the problem and irregularity of plasma profile.

3. The Integrated Tokamak Modelling Task Force

The Integrated Tokamak Modelling Task Force (ITM-TF) was created in 2003 to coordinate development of a coherent set of European simulation tools to be benchmarked on existing tokamak experiments, with the ultimate aim of providing a validated simulation package for ITER exploitation. The ITM-TF is divided into four Integrated Modelling Projects (IMPs) focused on the following areas of physics: plasma equilibrium and MHD, transport code and whole discharge evolution, transport and micro-instabilities, and finally, heating, current drive (H&CD) and fast particles. Their work programmes reflect some of the needs expressed by ITER, most of which require an Integrated Modelling platform [6]:

- IMP12: MHD equilibrium, stability and disruptions;
- IMP3: Transport Code and Discharge Evolution;
- MP4: Transport Processes and Micro stability;
- IMP5: Heating, Current Drive, and Fast Particle Physics;
- ISIP: Infrastructure and Software Integration Project

A central ITM-TF project is the development of the European Transport Solver (ETS) [10]. This is motivated by the fact that none of the existing transport codes such as: ASTRA, JETTO, CRONOS or TRANSP, did not meet all of the ITM requirements, namely modularity, flexibility and standarized interfaces. A schematic view of the ETS workflow is show in Fig. 3.
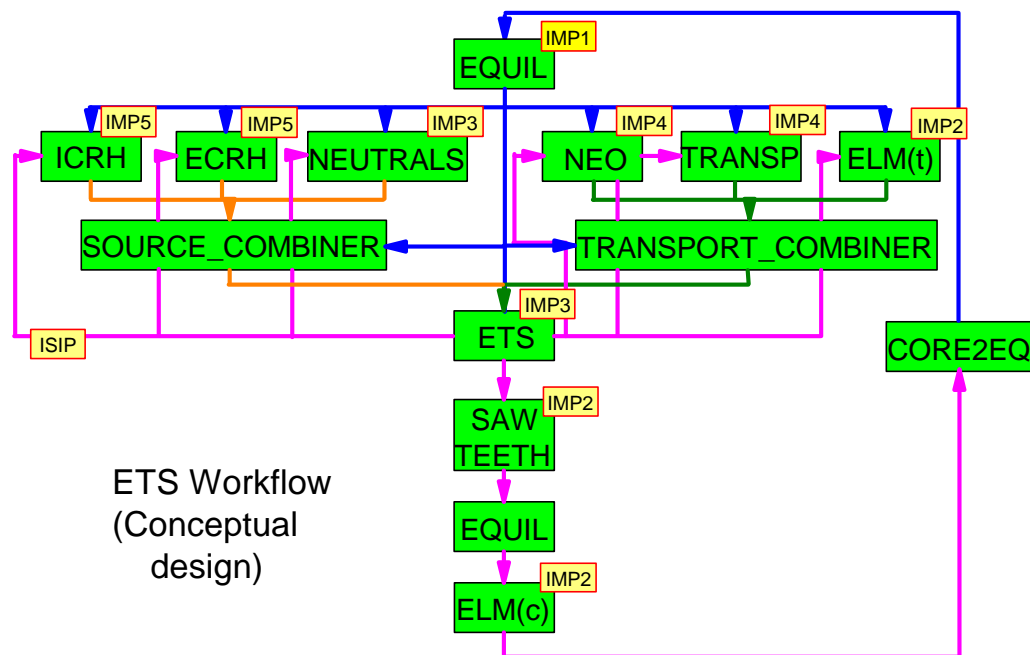

Fig. 3. Simplified version of one of the planned physic workflows.

4. The European Transport Solver

The European Transport Solver (ETS) is a new 1-D core transport code being developed by members of Integrated Modelling Project 3 (Transport Code and Discharge Evolution) of the European Fusion Development Agreement (EFDA) Task Force on Integrated Tokamak Modelling [6, 10]. Its objective is to develop a tokamak transport code able to complete simulation of the discharge in a tokamak like ITER including the core, the edge and the scrape-off layer. Such simulator should adopt a modular approach, where standing alone physics and numeric modules are communicating to each other via standardized interfaces linked with the ITM agree data structure. The schematic view of the ETS is shown in Fig. 4. This construction should allow on easy incorporating or replacing various physics modules of different levels of completeness and complexity, necessary for preparing and analyzing future fusion reactors, with the highest degree of flexibility and reliability.

In terms of the physics, the ETS is designed to solve the standard set of one-dimensional time-dependent equations which describe the evolution of the core plasma [11], including several ion species (impurities), plasma current, ion densities, ion and electron temperatures and ion toroidal velocity [12]. All equations are written in the standard generic form for an unknown function Y:

$$\frac{a(\rho) \cdot Y(\rho,t) - b(\rho) \cdot Y_{(-1)}(\rho,t)}{h} =$$

$$-\frac{1}{c(\rho)}\frac{\partial}{\partial \rho}\left(-d(\rho)\cdot\frac{\partial Y(\rho,t)}{\partial \rho} + e(\rho)\cdot Y(\rho,t)\right) + f(\rho) - g(\rho)\cdot Y(\rho,t) \tag{3}$$

and with boundary conditions

$$v(\rho_{bnd}) \cdot \left.\frac{\partial Y(\rho,t)}{\partial \rho}\right|_{bnd} + u(\rho_{bnd}) \cdot Y(\rho_{bnd},t) = w(\rho_{bnd}) \tag{4}$$

where $v(\rho_{bnd})$, $u(\rho_{bnd})$ and $w(\rho_{bnd})$ are coefficients required by the solver, ρ is the normalized radius of the tokamak core ($0 \leq \rho \leq 1$), h is time step and the coefficients of the equation, $a,...,g$, depend on a particular function Y, where $Y_{(-1)}(\rho,t)$ is taken at the previous time step. One can expect that in different situations, different numeric methods will be more suitable. This is the reason why several numerical methods have been implemented as subroutines into the ETS. The coupling between equations is included in the coefficients and is resolved by running an iteration after each time step. The European Transport Solver will be able to treat several ion components, ultimately including all impurity species and ability to use stiff transport models within a reasonable CPU time [10, 12, 13].
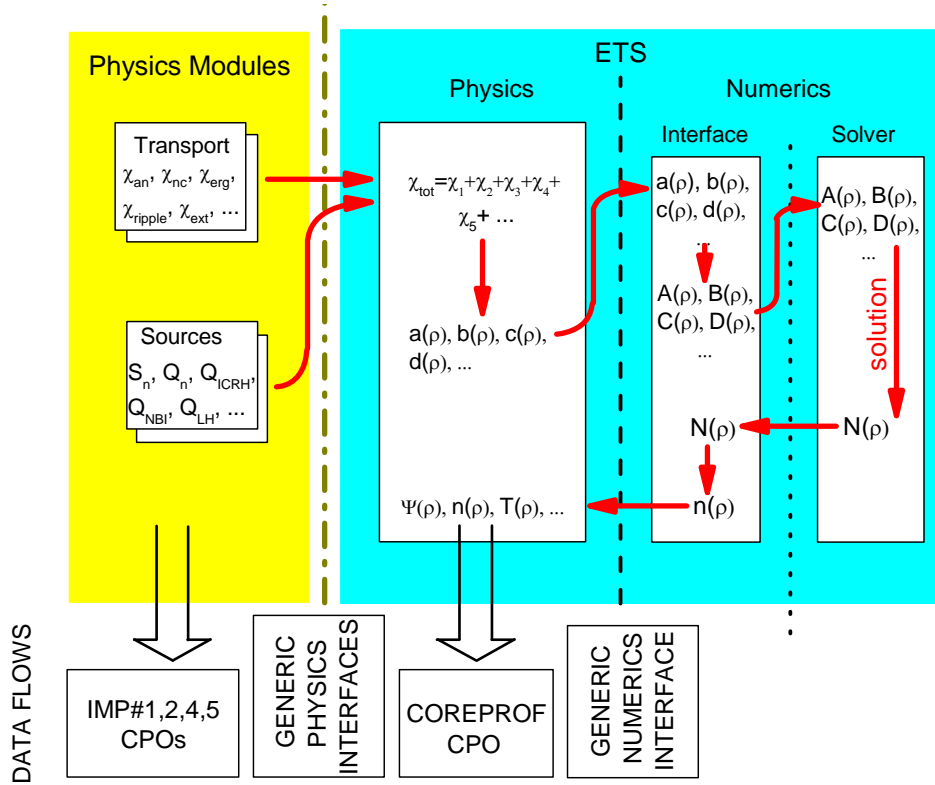
Fig. 4. Modular structure of the ETS. The sources and the transport coefficients are calculated externally, and there is also a separation between the physics and the numerics.

The solver itself is designed with a modular approach enabling the separation of the numerics from the physics, thereby facilitating the testing/usage of the numerical schemes that best suit a particular scenario. The ETS workflows are designed to be completely modular allowing the exchange of any component by any other of the same class. Internally the ETS is also modular separating the physic part and the numerical part. Communication between physic modules and the ETS is organized by generic physic interfaces such as TRANSPORT and SOURCE. The aim of this interfaces is to pass physical parameters into the form of explicit (independent on the variables used in transport equations) and implicit terms (proportional to the density, temperature and etc.). The role of the generic numeric interface is to communicate numerical coefficients derived by the physics part with the numeric part of the ETS. Since different numerical solvers are used with ETS, the interface in the numeric part translate generalized coefficient to internal coefficient used by the particular solver. In some cases the physical variable used by numerical solver is different from the one in physic equation. For instance the solution for the total number of particle, $N(\rho)$, within a certain flux surface is stead of density of particle, $n(\rho)$, at this flux surface can be the output of numeric solver. In this case, a translation back to the quantity required by physics part is done [13, 14].

5. ETS testing

The first group of tests deal with a reduce set of transport equations in a simplified cylindrical geometry treaded by a strongly non-linear stiff transport model which describes tokamak transport driven by plasma micro-turbulences. Suppression of the turbulence manifests itself by a dramatic reduction of the transport in some plasma regions. Such change of the transport leads to strong gradients of the plasma profiles. In our model the manufactured method of

analytical solution generation was developed for discontinuous model of diffusion coefficients depending on e-folding length as the Internal Transport Barrier (ITB) simple approximation. The goal of verification was to check the numerical methods used in the ETS and extend the method of verification to a continuous model of the diffusion coefficient [15]. The tests were performed in order to check whether the numerical procedure implemented in the ETS can reproduce position of the transport barrier and its dynamics given by analytical solutions. The ETS physics model contain standard 1-D core transport equations. One of them is the time dependent ion diffusion equation:

$$\left(\frac{\partial}{\partial t} - \frac{\dot{B}_0}{2B_0} \cdot \frac{\partial}{\partial \rho} \rho \right)(V'n_i) + \frac{\partial}{\partial \rho} \Gamma_i = V'\left(S_{i,\exp} - S_{i,imp} \cdot n_i \right) \tag{5}$$

where B_0 is magnetic field at the reference position, $V' = \partial V / \partial \rho$ (V is plasma volume), $S_{i,\exp}$ and $S_{i,imp}$ are explicit and implicit parts of the ion particle sources, the total ion flux is defined as: $\Gamma_i = V'\left\langle |\nabla \rho|^2 \right\rangle \left(-D_i \frac{\partial n_i}{\partial \rho} + n_i V_i^{pinch} \right)$, V_i^{pinch} is ion pinch velocity.

In order to verify if the analytical solutions can be reproduced correctly by the numerical solvers implemented into the ETS, equation (5) was rewritten in cylindrical geometry: $\left\langle |\nabla \rho|^2 \right\rangle = 1$, under assumptions that $\dot{B}_0 = 0$ (no compression), $V_i^{pinch} = 0$ (no particle pinch) and $S_{i,imp} = 0$ (no implicit source), $V' = \rho$. In this way equation (5) was simplified to the following form:

$$\frac{\partial(\rho n_i)}{\partial t} - \frac{\partial}{\partial \rho}(\rho D_i \frac{\partial n_i}{\partial \rho}) = \rho Q \ , \ \ \rho \in [0,1] \tag{6}$$

where the function n_i can be interpreted as a profile of plasma density or temperature, D_i is the diffusion coefficient, and Q is the source term. The function n_i depends on time t and normalized radius ρ.

For the ETS testing needs a simple transport model was adopted. In this model the diffusion coefficients changes abruptly when the temperature e-folding length, $L_T \equiv -dr / d \ln T$, approaches to the critical value L_{cr} [16], which represents the Internal Transport Barrier (ITB) position and is taken arbitrary. For some value of the e-folding length the diffusion coefficient D_i is defined by the following inequalities:

$$D_i = D_1 \ \text{ for } \ -\frac{n_i}{(\partial n_i / \partial \rho)} > L_{cr}$$

$$\tag{7}$$

and

$$D_i = D_2 << D_1 \ \text{ for } \ -\frac{n_i}{(\partial n_i / \partial \rho)} < L_{cr}$$

The value of ρ for which the diffusion coefficient is discontinuous is denoted as ρ_{cr}. This simplified formulation of the problem should allow for deeper understanding of the difficulty in solving the stiff transport problem. The obtained numerical solutions were compared with analytical ones.

The generation of solutions by using the manufactured solution method is based on inversion of the problem. We assume that the solution is given by a function sufficiently smooth and also the coefficients of the equation are defined as some smooth functions. Then, using the assumed form of the solution and coefficients we can calculate the source term from the considered equation (6). Due to discontinuity of the first derivative of the solution we introduce a smooth function f which corresponds to the flux function:

$$f = -D\frac{\partial n}{\partial \rho} \tag{8}$$

The derivative of the solution with respect to ρ is discontinuous at ρ_{cr}. It follows from the transport model (7) that ρ_{cr} satisfies the following inequalities:

$$\frac{L_{cr}}{D_2} < \frac{n(\rho_{cr},t)}{f(\rho_{cr},t)} < \frac{L_{cr}}{D_1} \tag{9}$$

If the function f is monotonically increasing, the solution of equation (9) exists for ρ_{cr} in some interval ($\rho_{cr.\min}$, $\rho_{cr.\max}$). The analytical solution corresponding to function f is defined in terms of function F given by:

$$f(\rho,t) = \frac{\partial F(\rho,t)}{\partial \rho} \tag{10}$$

Equation (8) leads to the solution with continuous flux and discontinuous gradient given by:

$$n(\rho,t) = \frac{F(\rho_{cr},t) - F(\rho,t)}{D_1} + \frac{F(1,t) - F(\rho_{cr},t)}{D_2} + n(1) \qquad \text{for} \quad \rho < \rho_{cr} \tag{11a}$$

$$n(\rho,t) = \frac{F(1,t) - F(\rho,t)}{D_2} + n(1) \qquad \text{for} \quad \rho \geq \rho_{cr}, \tag{11b}$$

where for $\rho = 1$ function $n(\rho,t) \to n(\rho)$ is time independent and represents the boundary condition, for the source Q defined as:

$$Q(\rho,t) = Q_1(\rho,t) + Q_2(\rho,t) + Q_3(\rho,t) \tag{12}$$

where for all ρ:

$$Q_1 = \frac{f(\rho,t)}{\rho} + \frac{\partial f(\rho,t)}{\partial \rho} \tag{13}$$

whereas for $\rho < \rho_{cr}$:

$$Q_2 = \frac{\partial}{\partial t}\left[\frac{(F(\rho_{cr},t)-F(\rho,t))}{D_1} + \frac{(F(1,t)-F(\rho_{cr},t))}{D_2}\right] \qquad (14a)$$

$$Q_3 = \left\{\frac{\partial}{\partial \rho_{cr}}\left[\frac{F(\rho_{cr},t)-F(\rho,t)}{D_1}\right] + \frac{\partial}{\partial \rho_{cr}}\left[\frac{F(1,t)-F(\rho_{cr},t)}{D_2}\right]\right\}\frac{\partial \rho_{cr}}{\partial t}, \qquad (14a)$$

and for $\rho \geq \rho_{cr}$:

$$Q_2 = \frac{\partial}{\partial t}\left[\frac{F(1,t)-F(\rho,t)}{D_2}\right] \qquad (15a)$$

$$Q_3 = 0. \qquad (15b)$$

This solution satisfies the boundary condition at $\rho=0$ under the assumption that $f(0,t)=0$. In the above form of the solution the boundary condition at $\rho=1$ corresponds to the assumption that the value of the solution at $\rho=1$ is given. It is easy to replace this boundary condition by the condition imposed on value L_n of the e-folding length at $\rho=1$, using the following relation:

$$n(1) = \frac{L_n f(1)}{D_2} \qquad (16)$$

For f constant in time the function n defined by (10a) and (10b) satisfies the stationary diffusion equation with Q given by Q_1. Let us consider the stationary diffusion equation with $Q = S$ as an example. In this case $\rho_{cr.min}$ and $\rho_{cr.max}$ can be expressed by the formula:

$$\rho_{cr.min} = \sqrt{1 + \frac{4D_2 n(1)}{S} + L_{cr}^2} - L_{cr} \qquad (17a)$$

$$\rho_{cr.max} = \sqrt{1 + \frac{4D_2 n(1)}{S} + \left(L_{cr}\frac{D_2}{D_1}\right)^2} - L_{cr}\frac{D_2}{D_1}. \qquad (17b)$$

6. Numerical results

Nowadays several numeric procedures called "solvers" were implemented into the ETS. They are labeled by numbers 1, 2, 3, 6 and 7. Each solver has to be tested for a different set of transport models and sources. This paper presents some of the most important tests.

6.1. Constant stationary source

In this case a simple radially constant source was taken: $Q = S$. For this type of source the analytic flux $f = S\rho/2$. Equation (6) was solved with the help of solvers 1, 2, 3 and 7,

at initial condition given by the analytical function: $L_{cr} = 0.8$, $D_2 = 0.5$, $D_1 = 1$, $S = 4$ and three different boundary conditions at the edge:

type 1 (value): $n_i\big|_{\rho=\rho_{bnd}} = n_{i,bnd}$,

type 3 (scale length): $\dfrac{1}{(\partial \ln n_i / \partial \rho)}\bigg|_{\rho=\rho_{bnd}} = -L_{ni}$,

type 5 (generic): $v_{gen}\dfrac{\partial n_i}{\partial \rho}\bigg|_{bnd} + u_{gen} n_{i,bnd} = w_{gen}$.

For this sets of parameters $\rho_{cr}(D_2) = 0.662$ and $\rho_{cr}(D_1) = 0.824$. Computations was provided for a different time steps, $\tau = t_\infty / M$ (where $t_\infty = 10\,\text{s}$, M is number of iteration), using N radial mesh points. The difference between the numerical solution and the analytical function is expressed as the relative error given by: $\delta n = \left|\dfrac{n^{cal} - n^{an}}{n^{an}}\right|$ where n^{cal} stands for the numerical solution and n^{an} is the analytical solution. The most interesting results are presented in Fig.5 to Fig.19. All results are presented using arbitrary units (a.u.). The solution (a.u.) can be interpreted as the plasma concentration n or temperature T profile.
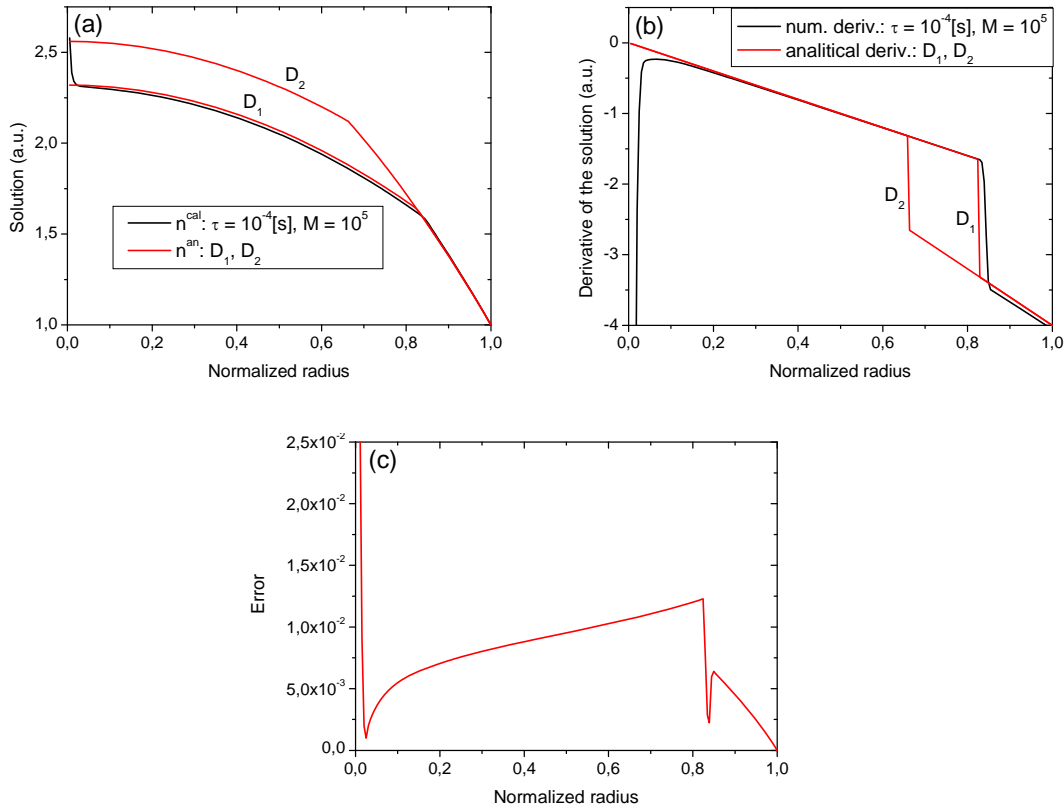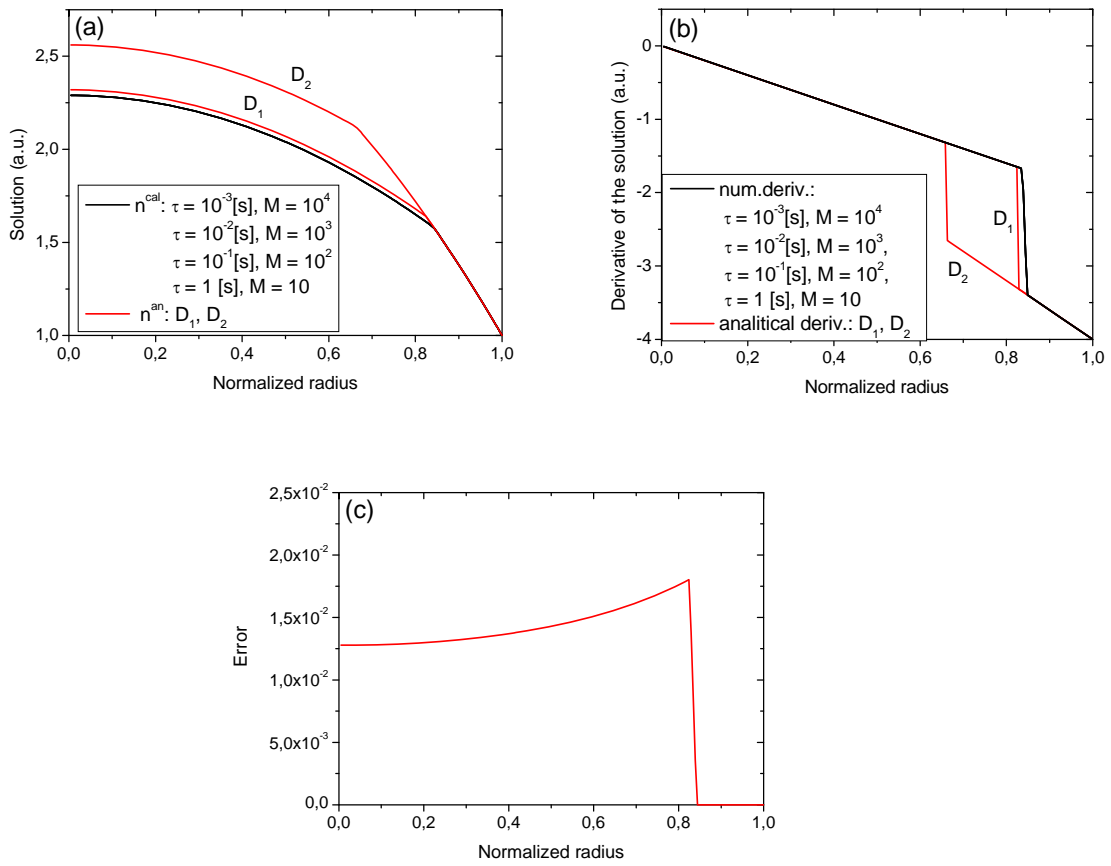

Fig. 5. Analytical solutions (red curves) and numerical solution (black curve) (a), their derivatives (b) and relative error (c) obtained for solver 1, boundary condition type 1 ($n_{i,bnd} = 1$) and $N = 200$.
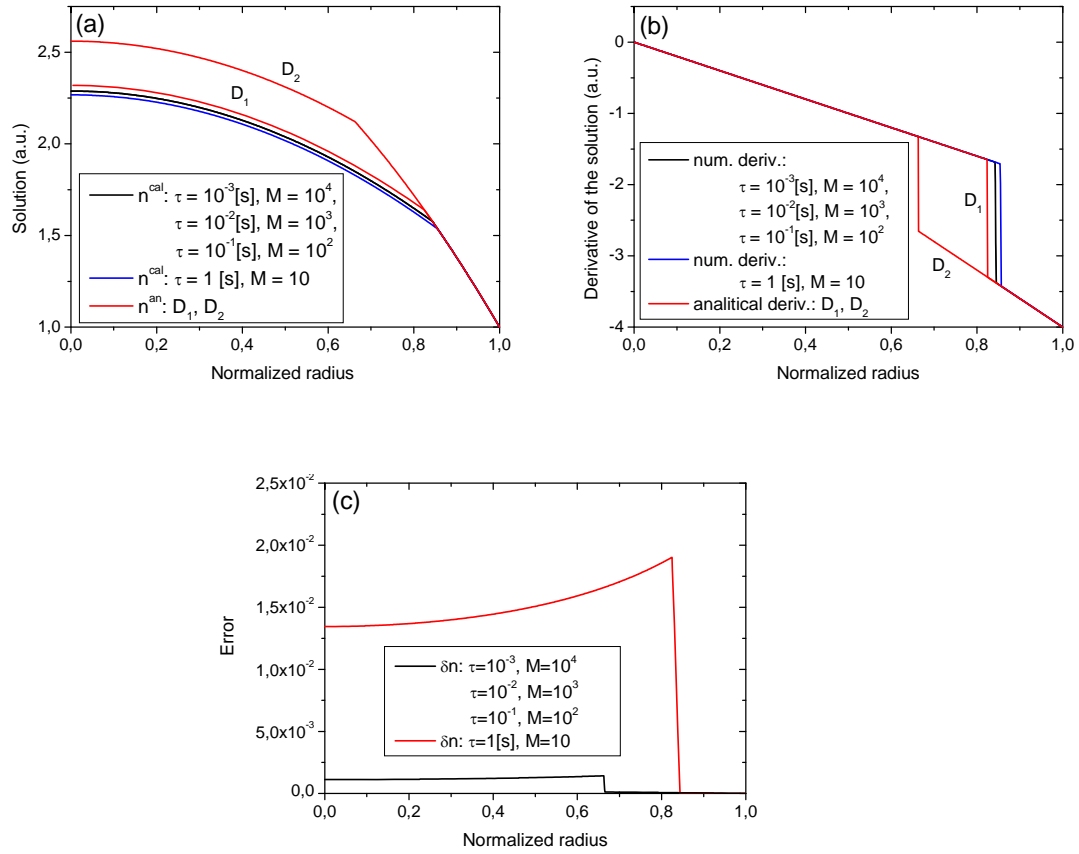
Analytical solutions should represent numeric ones after infinite number of the time steps. The aim is to find the most accurate time step τ and number N of the radial points after each numeric solution approach to the analytic one as close as possible. Derivatives of the analytical solution obtained for two different values of the diffusion coefficient D_1 and D_2 (red curves) indicate the bifurcation area, where the ITB is located. In this area the numerical solver has to make a choice between two different D_i values. In the cases of solver 1 (Fig. 5) the numerical solution was obtained for a very small time step $\tau = 10^{-4}$ s and radial points number $N = 200$. There was no solution for $N = 1000$. In Fig. 5a the numerical solution approaches to the analytic one obtained for D_1. The relative error (Fig. 5c) decreases for $\rho > \rho_{cr}(D_1) = 0.824$.

Fig. 6. Analytical solutions (red curves) and numerical solutions (black curves) (a), their derivatives (b) and relative error (c) obtained for solver 3, boundary condition type 1 ($n_{i,bnd} = 1$) and $N = 200$.
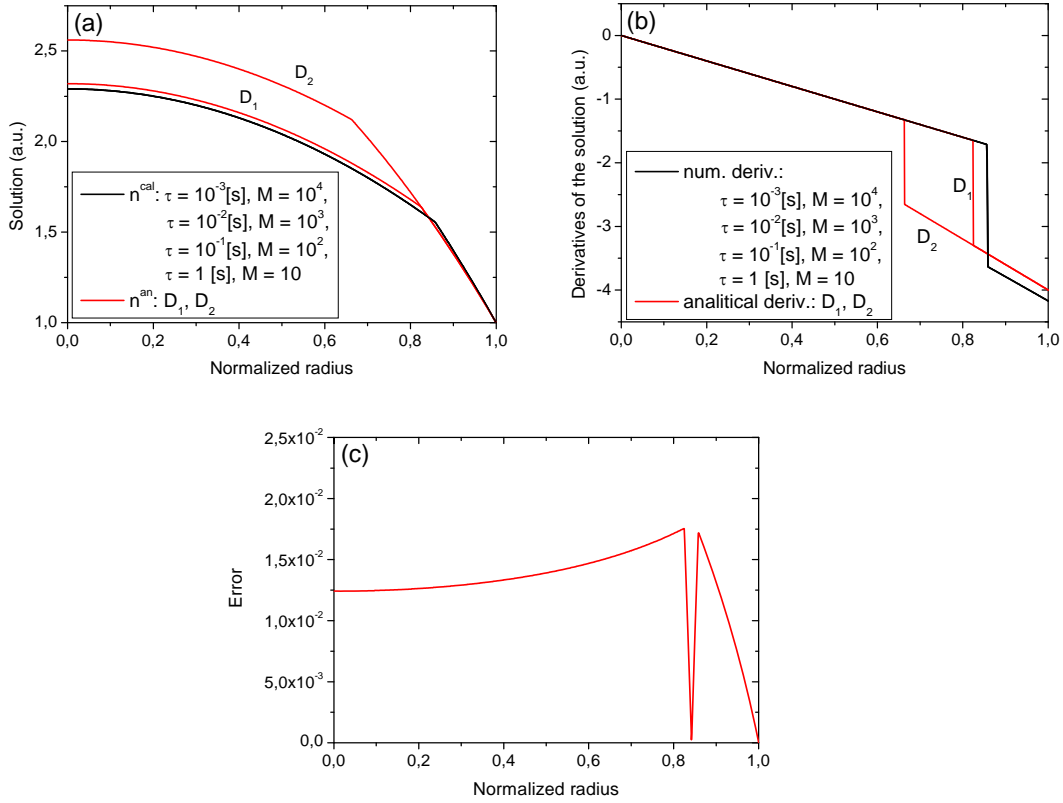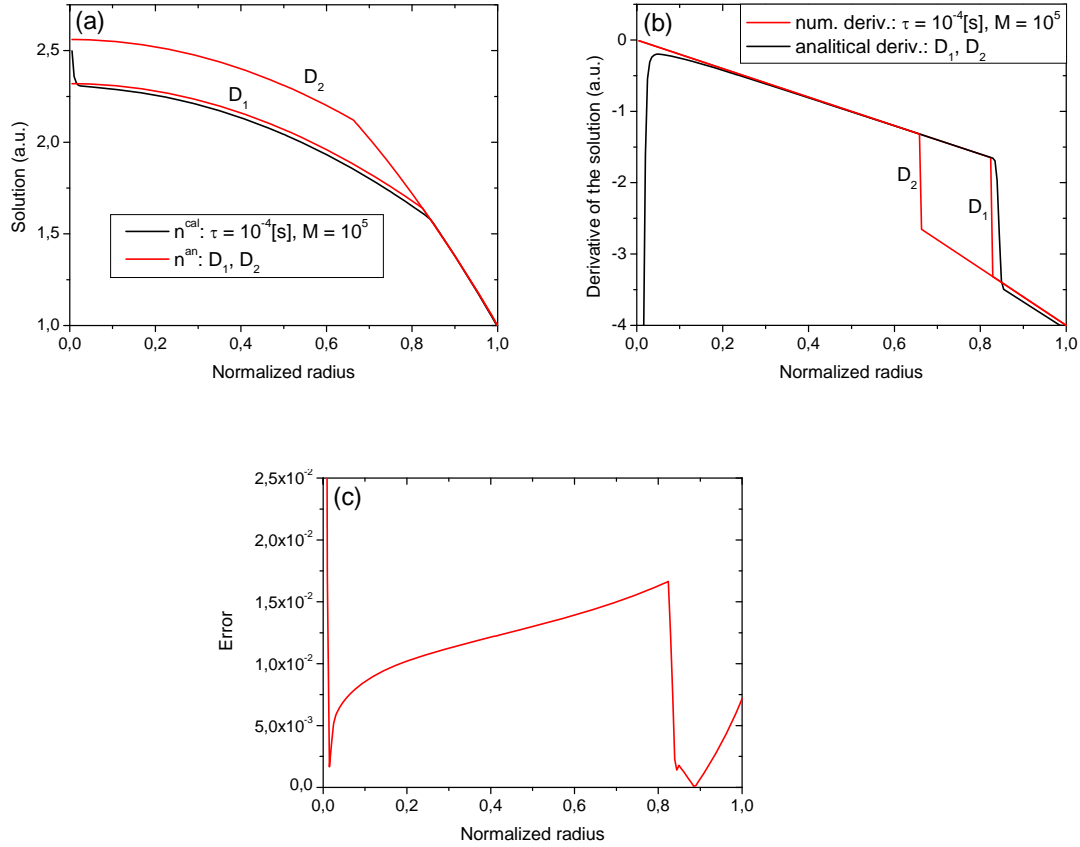
Fig. 7. Analytical solutions (red curves) and numerical solutions (black and blue curves) (a), their derivatives (b) and relative error (c) obtained for solver 3, boundary condition type 1 ($n_{i,bnd} = 1$) and $N = 1000$.

Results presented in Fig. 6 and Fig. 7 were obtained with the help of solver 3 using the boundary condition type 1. The numerical solution represented by the blue curve (Fig. 7a), being significantly differ from the rest of the numerical solutions, was obtained for the biggest time step $\tau = 1\,\mathrm{s}$ and $N = 1000$ radial points. In this case the relative error is slightly higher then those obtained for $N = 200$.
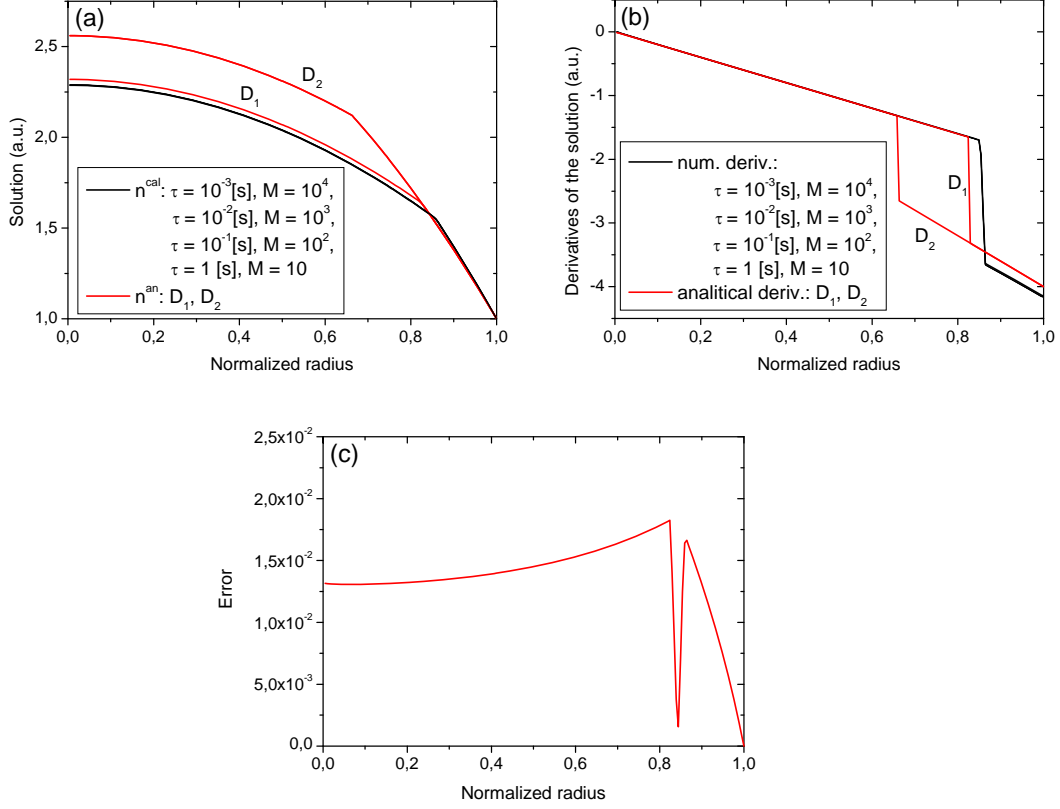
Fig. 8. Analytical solutions (red curves) and numerical solutions (black curves) (a), their derivatives (b) and relative error (c) obtained for solver 7, boundary condition type 1 ($n_{i,bnd} = 1$) and $N = 200$.
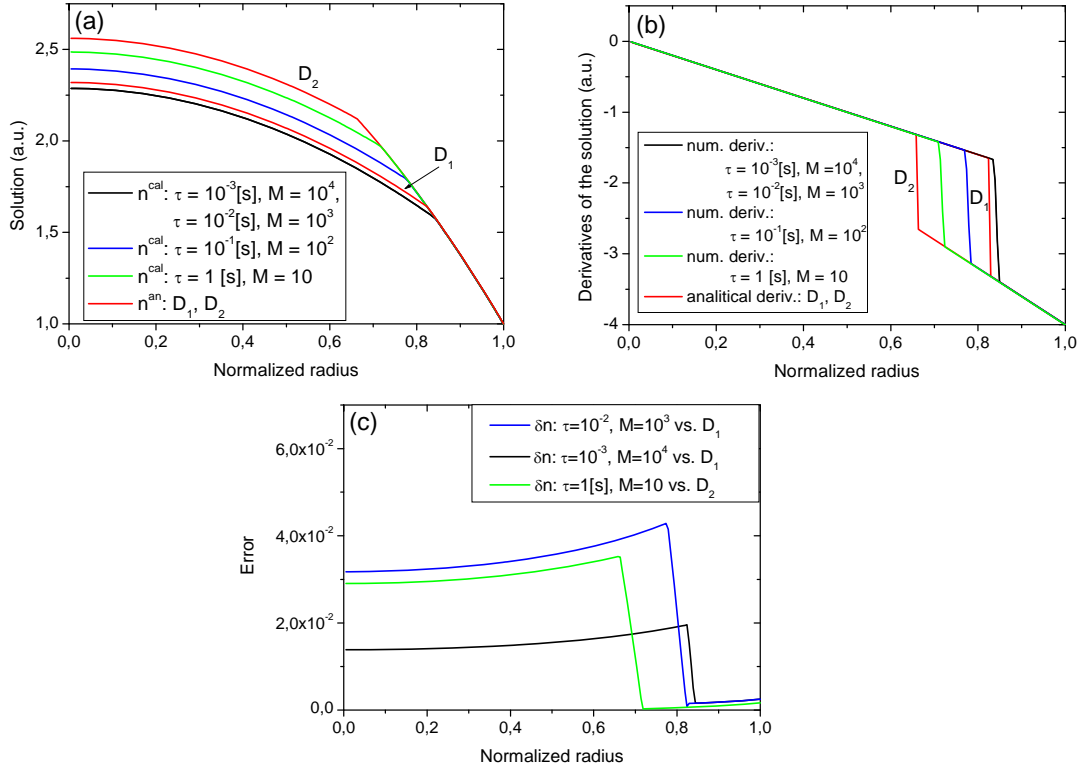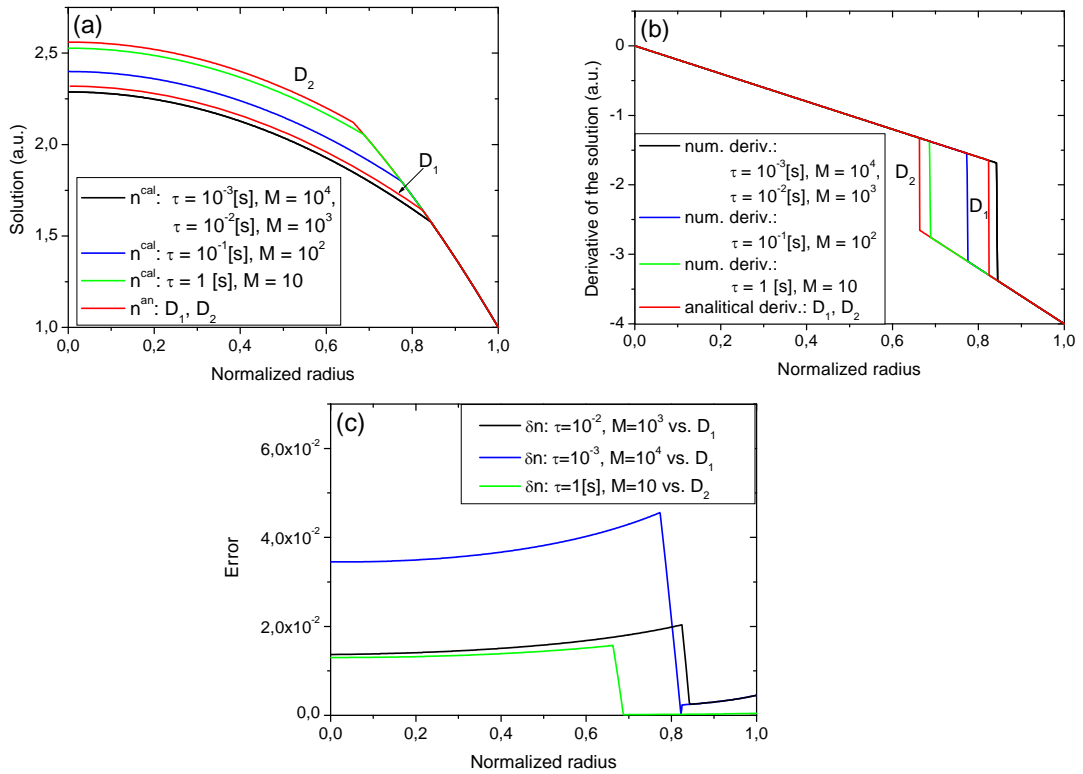

Fig. 9. Analytical solutions (red curves) and numerical solution (black curve) (a), their derivatives (b) and relative error (c) obtained for solver 7, boundary condition type 1 ($n_{i,bnd} = 1$) and $N = 1000$.

The results presented in Fig. 8 and Fig. 9 were obtained with the help of solver 7 and boundary condition type 1, radial points: $N = 200$ and $N = 1000$. In this case the numerical solutions found for a different time step τ seems to be close to each other. The relative error (Fig. 8c, 9c) decreases for $\rho > \rho_{cr}(D_1)$ but much slower than for solver 3 (Fig. 6c, 7c).

Fig. 10. Analytical solutions (red curves) and numerical solution (black curve) (a), their derivatives (b) and relative error (c) obtained for solver 1, boundary conditions type 3 ($L_{ni} = 0.25$) and $N = 200$.

The results presented in Fig. 10 were obtained for a very small time step $\tau = 10^{-4}$ s. No solutions was obtained for a higher time step. This case is very similar to the previous case (Fig. 5) obtained for the same solver 1 but for a different boundary condition (type 1).
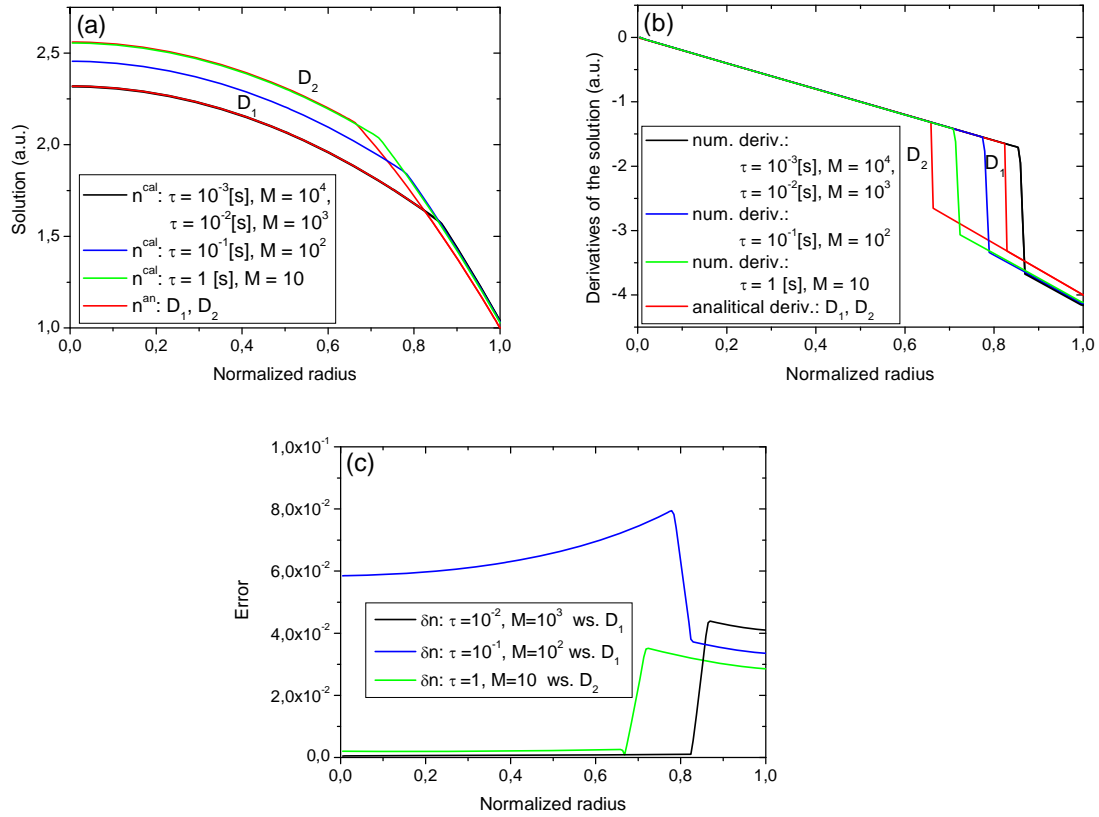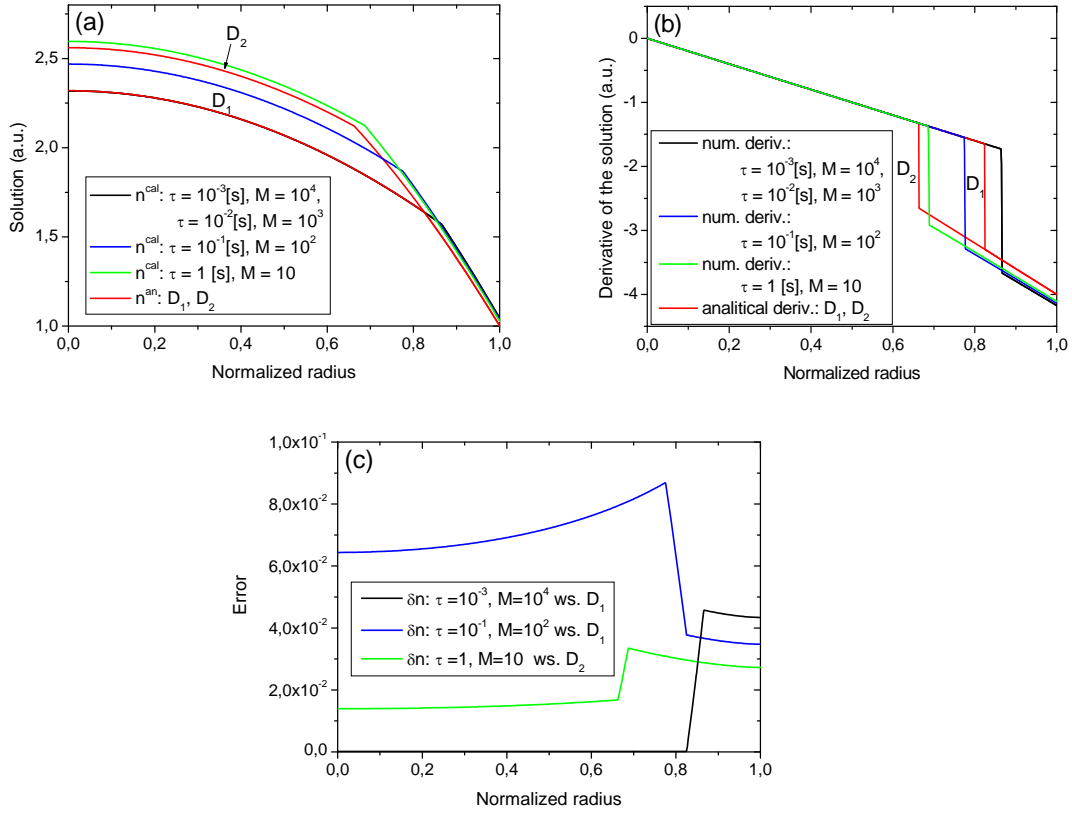
Fig. 11. Analytical solutions (red curves) and numerical solutions (black, blue and green curves) (a), their derivatives (b) and relative error (c) obtained for solver 3, boundary conditions type 3 ($L_{ni} = 0.25$) and $N = 200$.

Fig. 12. Analytical solutions (red curves) and numerical solutions (black, blue and green curves) (a), their derivatives (b) and relative error (c) obtained for solver 3, boundary conditions type 3 ($L_{ni} = 0.25$) and $N = 1000$.

The results presented in Fig. 11 and Fig. 12 were obtained with the help of solver 3 and boundary condition type 3. The numerical solutions for $N = 1000$ radial points and time step $\tau = 1$ s (Fig. 12a) present a smaller error then this for $N = 200$ (Fig. 11a).

Fig. 13. Analytical solutions (red curves) and numerical solutions (black, blue and green curves) (a), their derivatives (b) and relative error (c) obtained for solver 7, boundary conditions type 3 ($L_{ni} = 0.25$) and $N = 200$.

Fig. 14. Analytical solutions (red curves) and numerical solutions (black, blue and green curves) (a), their derivatives (b) and relative error (c) obtained for solver 7, boundary conditions type 3 ($L_{ni} = 0.25$) and $N = 1000$.

The results presented results in Fig. 13 and Fig. 14 were obtained with the help of solver 7 and boundary condition type 3.
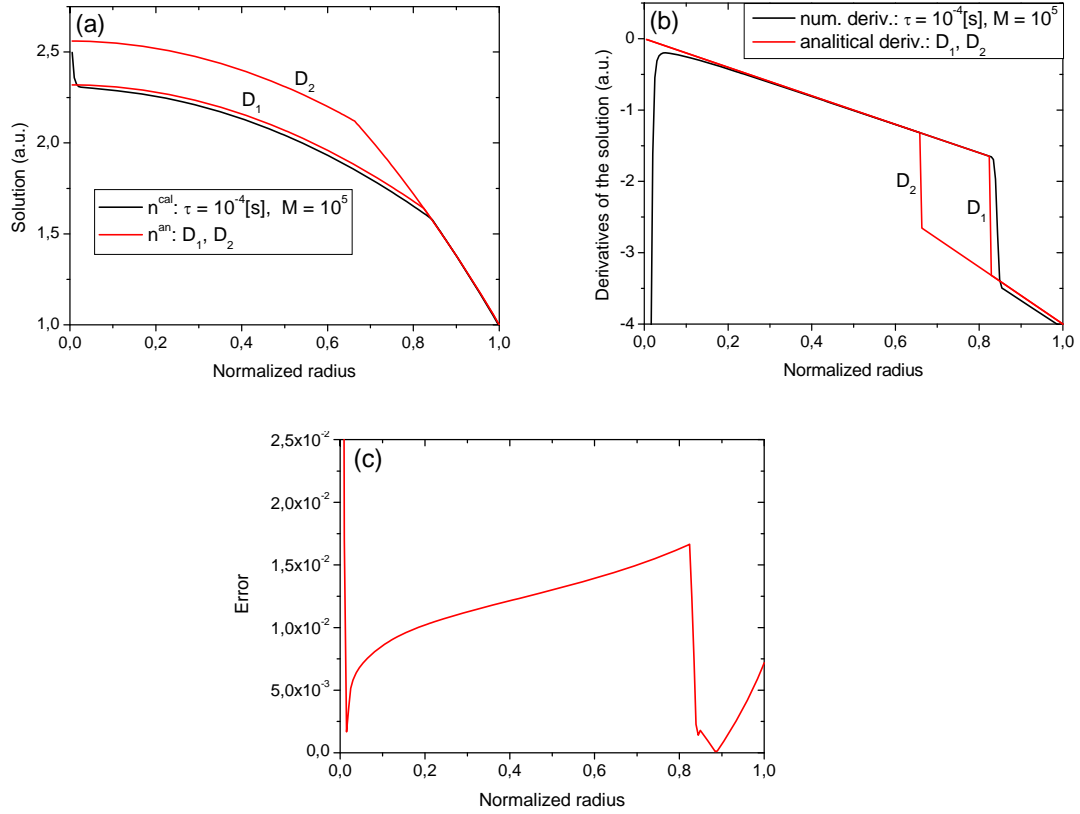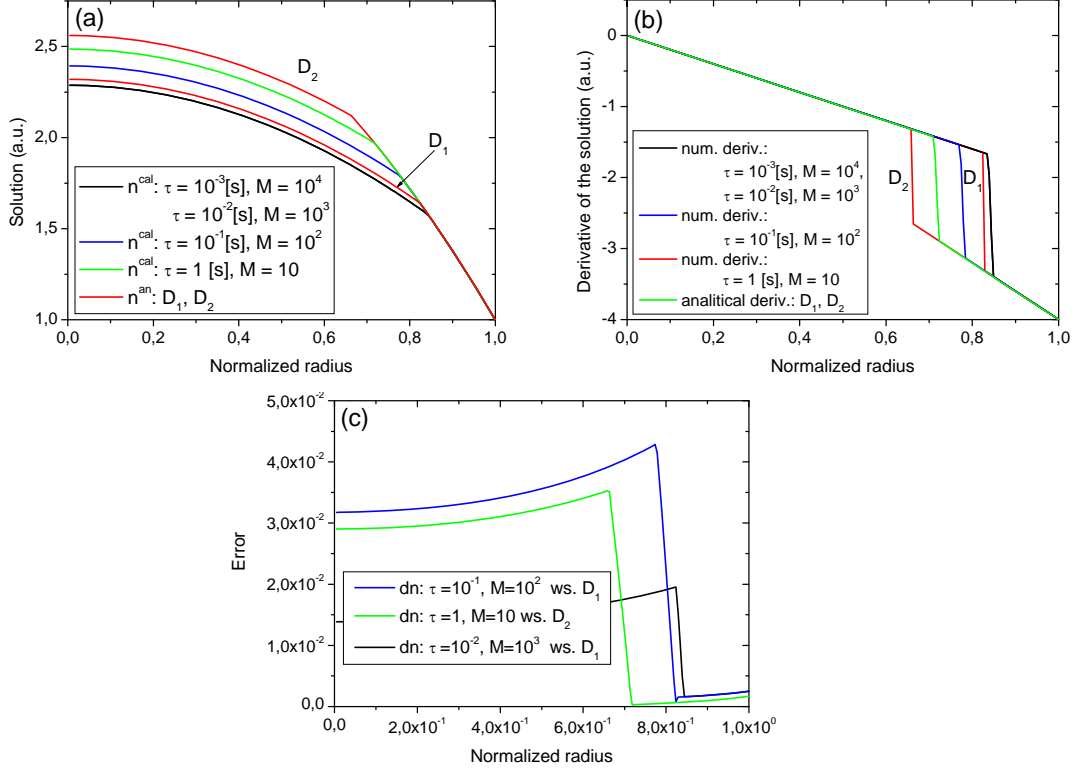
Fig. 15. Analytical solutions (red curves) and numerical solution (black curve) (a), their derivatives (b) and relative error (c) obtained for solver 1, boundary conditions type 5 ($v_{gen} = 0.25$, $u_{gen} = 1$, $w_{gen} = 0$) and $N = 200$.

The results presented in Fig. 15 were obtained with the help of solver 1 and boundary condition type 5. The numerical solution was obtained only for a very small time step $\tau = 10^{-4}$ s and $N = 200$ radial points, but no solutions was obtained for a higher time step τ or higher N. This situation is typical for solver 1 which was tested for different boundary conditions (Fig. 5 and Fig. 10).

Fig. 16. Analytical solutions (red curves) and numerical solution (black, blue and green curves) (a), their derivatives (b) and relative error (c) obtained for solver 3, boundary conditions type 5 ($v_{gen} = 0.25$, $u_{gen} = 1$, $w_{gen} = 0$) and $N = 200$.
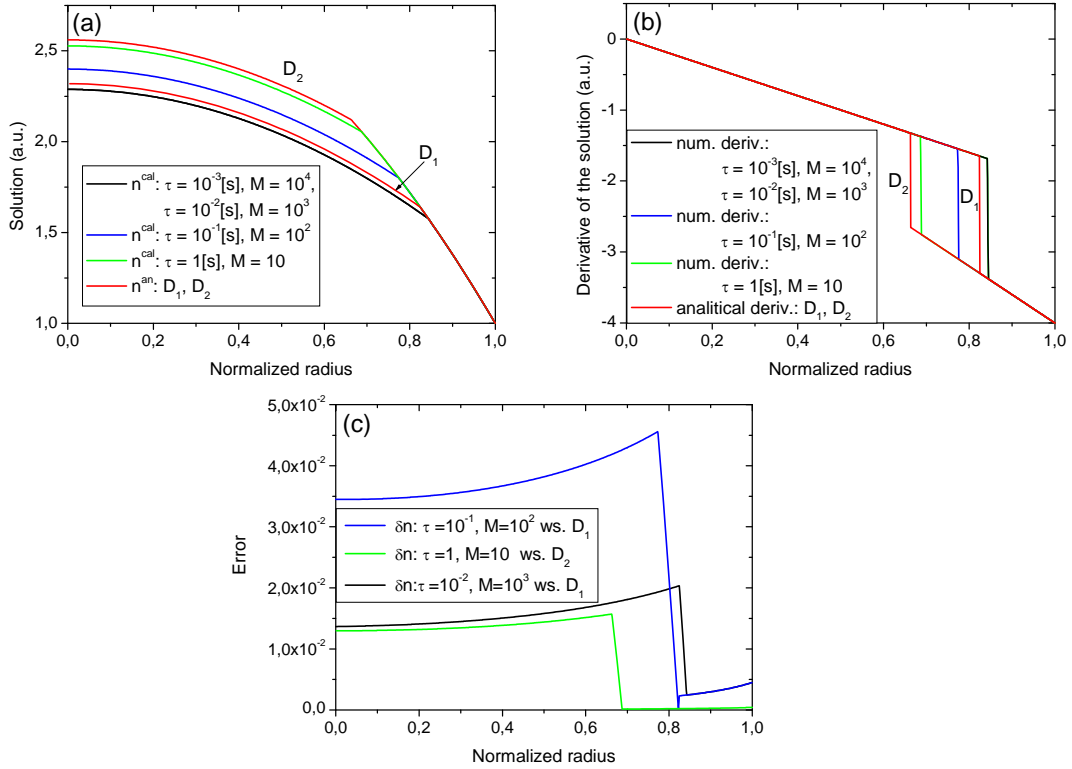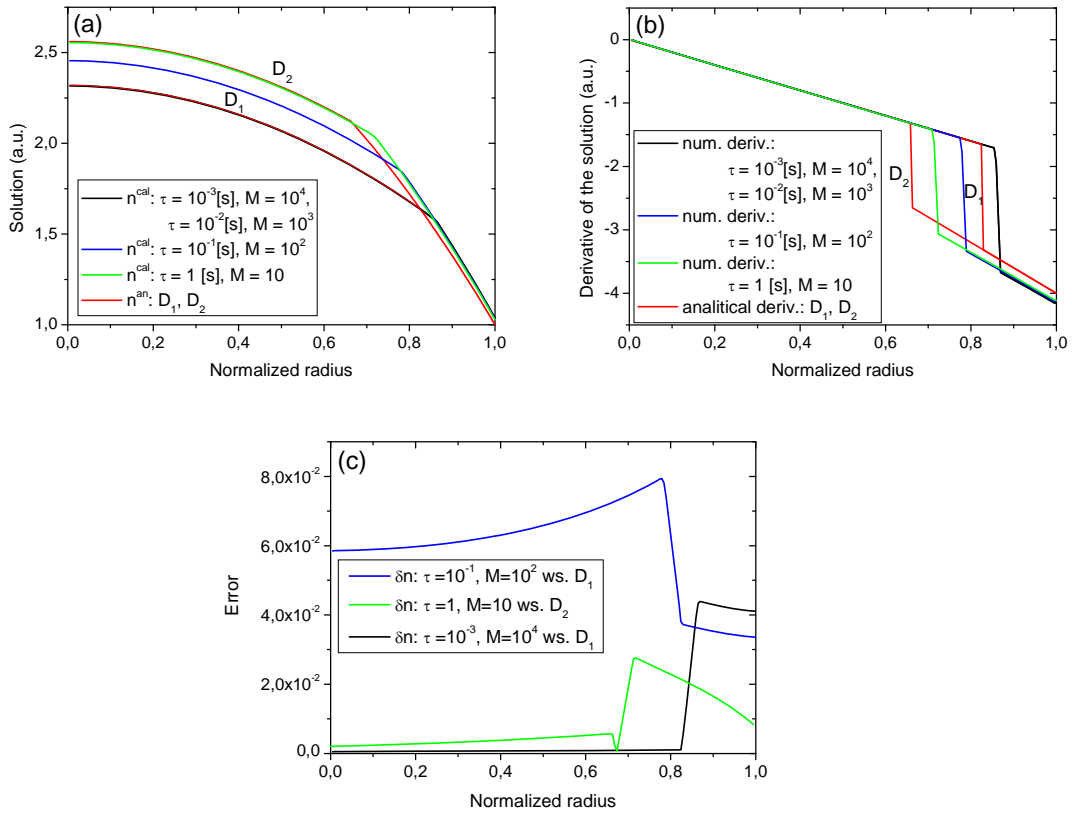

Fig. 17. Analytical solutions (red curves) and numerical solutions (black, blue and green curves) (a), their derivatives (b) and relative error (c) obtained for solver 3, boundary conditions type 5 ($v_{gen} = 0.25$, $u_{gen} = 1$, $w_{gen} = 0$) and $N = 1000$.

20

Numerical solutions obtained for $N = 1000$ radial points (Fig. 17) present a better match to the analytical solution then those obtained for only $N = 200$ radial points (Fig. 16).
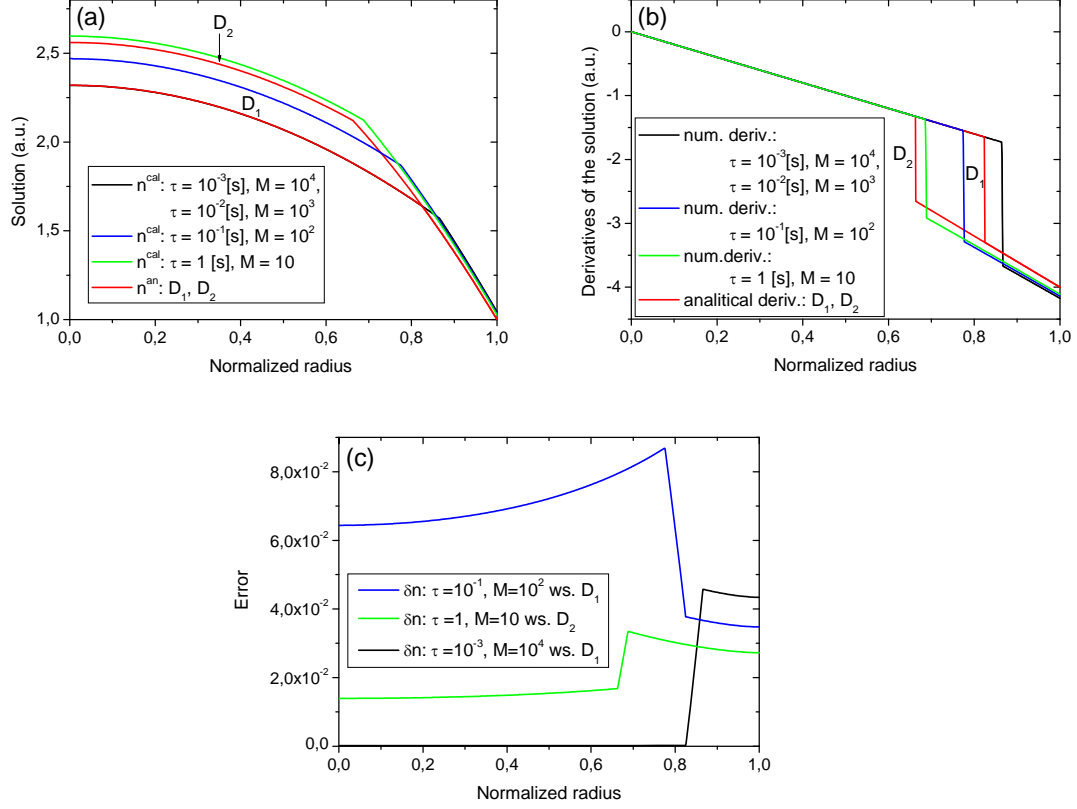

Fig. 18. Analytical solutions (red curves) and numerical solutions (black, blue and green curves) (a), their derivatives (b) and relative error (c) obtained for solver 7, boundary conditions type 5 ($v_{gen} = 0.25$, $u_{gen} = 1$, $w_{gen} = 0$) and $N = 200$.

Fig. 19. Analytical solutions (red curves) and numerical solutions (black, blue and green curves) (a), their derivatives (b) and relative error (c) obtained for solver 7, boundary conditions type 5 ($v_{gen} = 0.25$, $u_{gen} = 1$, $w_{gen} = 0$) and $N = 1000$.

Numerical solutions obtained with the help of solver 7 and boundary conditions type 1, 3 and 5 present bigger differences from the analytical solutions then those obtained with the help of solver 3. This difference is specially very well visible for $\rho > \rho_{cr}(D_i)$. In the case of solvers 3 and 7 it was possible to obtain a set of different numerical solutions passing through bifurcation area. A good convergence especially in case of solver 3 was possible to obtain by delicate time step selection. Solvers 3 and 7 are much more flexible then solver 1 where the only possible solution was obtained for a very small time step $\tau = 10^{-4}$ s and small numbers N of the radial points. In the case of solver 2 the numerical computations provided for different time steps and different numbers of the radial points gave no results.

6.2. Radially varying source

Second test was provided for a radially varing source $Q = S(1 - \rho^2)$. For this type of source the flux function f is defined as: $f = S(\rho/2 - \rho^3/4)$. Equation (6) was solved with the help of solver 3 and initial condition given by the analytical function: $L_{cr} = 0.8$, $D_2 = 0.5$, $D_1 = 1$ and boundary condition type 1. The calculation results obtained for $S = 6$ and $S = 8$ are plotted in Fig. 20a where numerical solutions remain close to the analytical one. In order to show the difference between the analytical and numerical solutions only the parts of curves close to the critical radius are presented in Fig. 20b. The difference between the numerical

solution and the analytical function used as its initial condition is presented in Fig. 20c. The relative error rapidly decreases when $\rho > \rho_{cr}$.
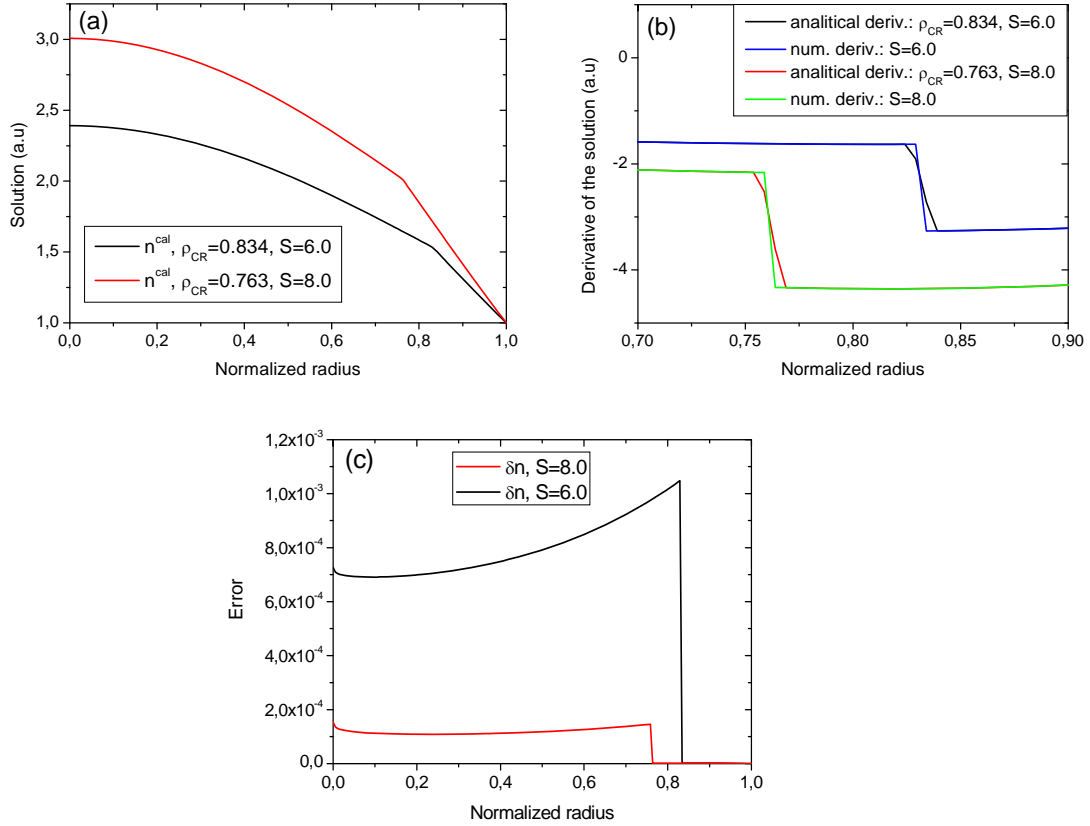

Fig. 20. Numerical solutions (a), their derivatives compare with the analytical one (b) and relative error (c) obtained for: $\tau = 10^{-4}$ s, $M = 10^5$ and $N = 200$.

The numerical solution converges to the analytical solution for critical radius equal to 0.763 ($S = 8$) and 0.834 ($S = 6$) as can be seen after studying the derivatives of the numerical solution in comparison with the derivatives of the analytical solutions at the critical radius defined by the numerical solution.

6.3. Time dependent source

Third test was provided for a time dependent source: $Q = S_0 + t\alpha$. For this type of source the flux function: $f = \rho(S_0 + t\alpha)/2$, where $S_0 = 3$, t = 10 s and $\alpha = 0.1\,\text{s}^{-1}$. The equation (6) was solved with the help of solvers 3 and 7 and initial condition given by the analytical function: $L_{cr} = 0.8$, $D_2 = 0.5$, $D_1 = 1$ and boundary condition type 1. Computations was provided for a time step: $\tau = t_\infty / M = 10^{-2}$ s, where $t_\infty = 10\,\text{s}$ and $N = 500$ radial points. In this case the critical radius is time dependent and will have to be evaluated for each time step.
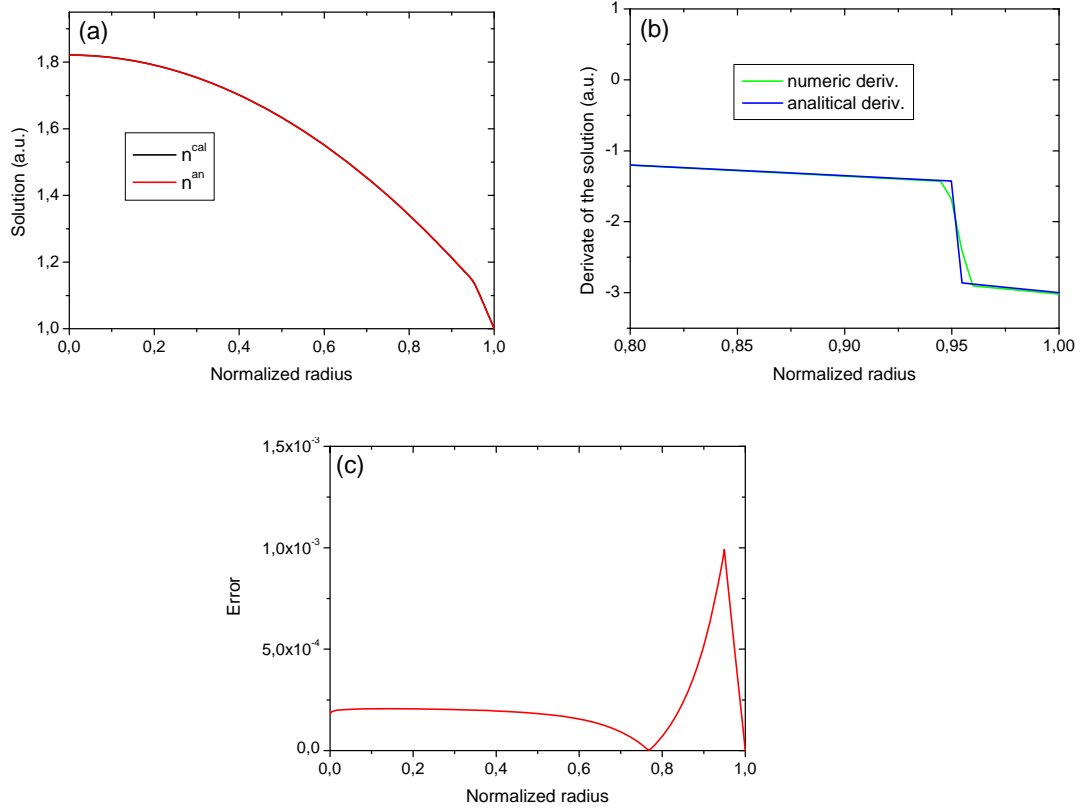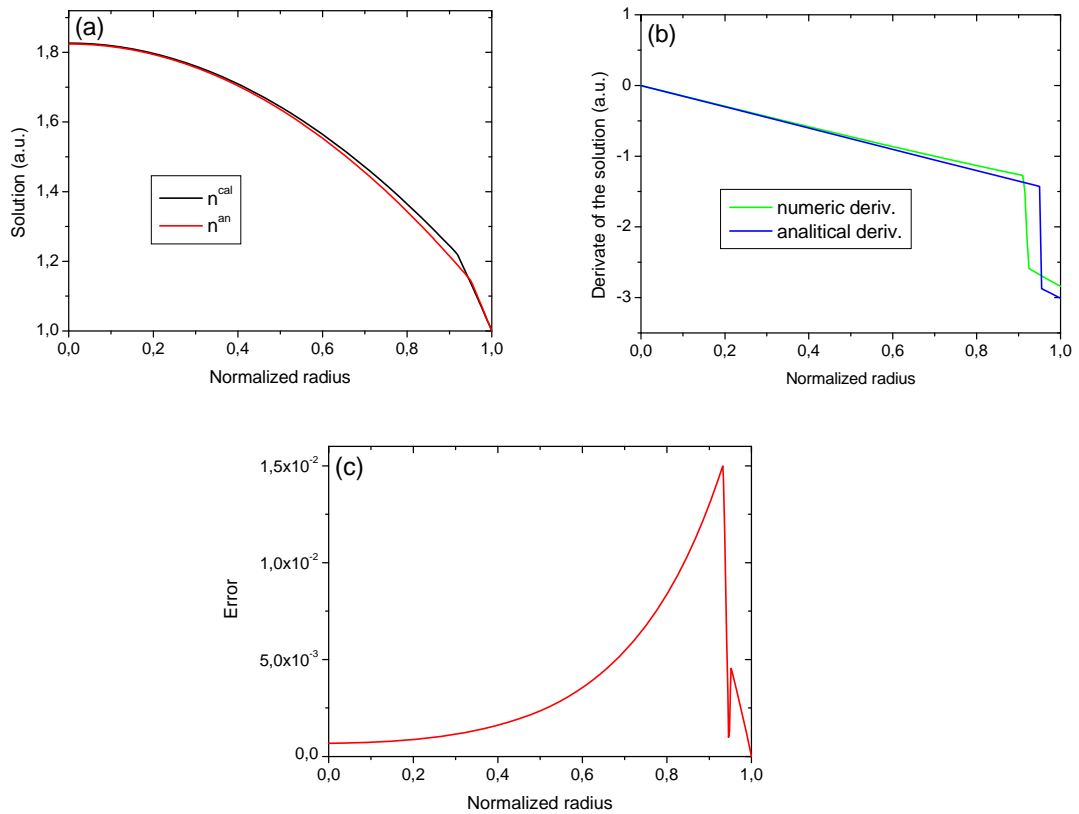
Fig. 21. Analytical and numerical solutions (a), their derivatives (b) and relative error (c) obtained for the first time step $\tau = 10^{-2}$ s, critical radius: $\rho_{cr}\left(\tau = 10^{-2}\,\text{s}\right) = 0.952$.
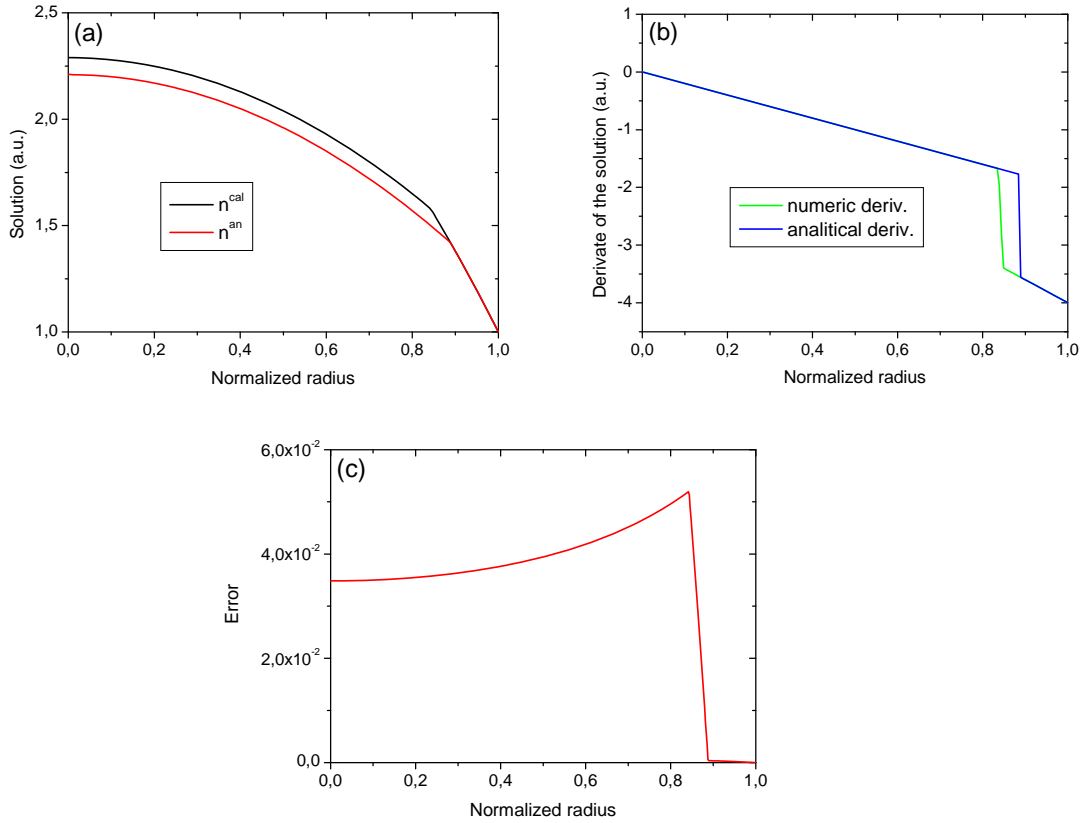

Fig. 22. Analytical and numerical solutions (a), their derivatives (b) and relative error (c) obtained for the tenth time step $\tau = 10^{-1}$ s, critical radius: $\rho_{cr}\left(\tau = 10^{-1}\,\text{s}\right) = 0.949$.

Fig. 23. Analytical and numerical solutions (a), their derivatives (b) and relative error (c) obtained for the last time step $\tau = 10\,\text{s}$, critical radius: $\rho_{cr}(\tau = 10\,\text{s}) = 0.886$.

The results presented in Fig. 21, 22, 23 were obtained with the help of solver 3. It can be seen that even for the first time step $\tau = 10^{-2}\,\text{s}$ (Fig. 21) the numerical solution differs significantly from the analytical one. For further time steps this difference has tendency to rise as it is visible in Fig. 22c and Fig. 23c where the errors are presented. Results obtained for the last time step $\tau = 10\,\text{s}$ (Fig. 23) show the highest differences between numerical and analytical solutions. Presented errors have tendency to rapidly decrease for $\rho > \rho_{cr}(\tau)$.
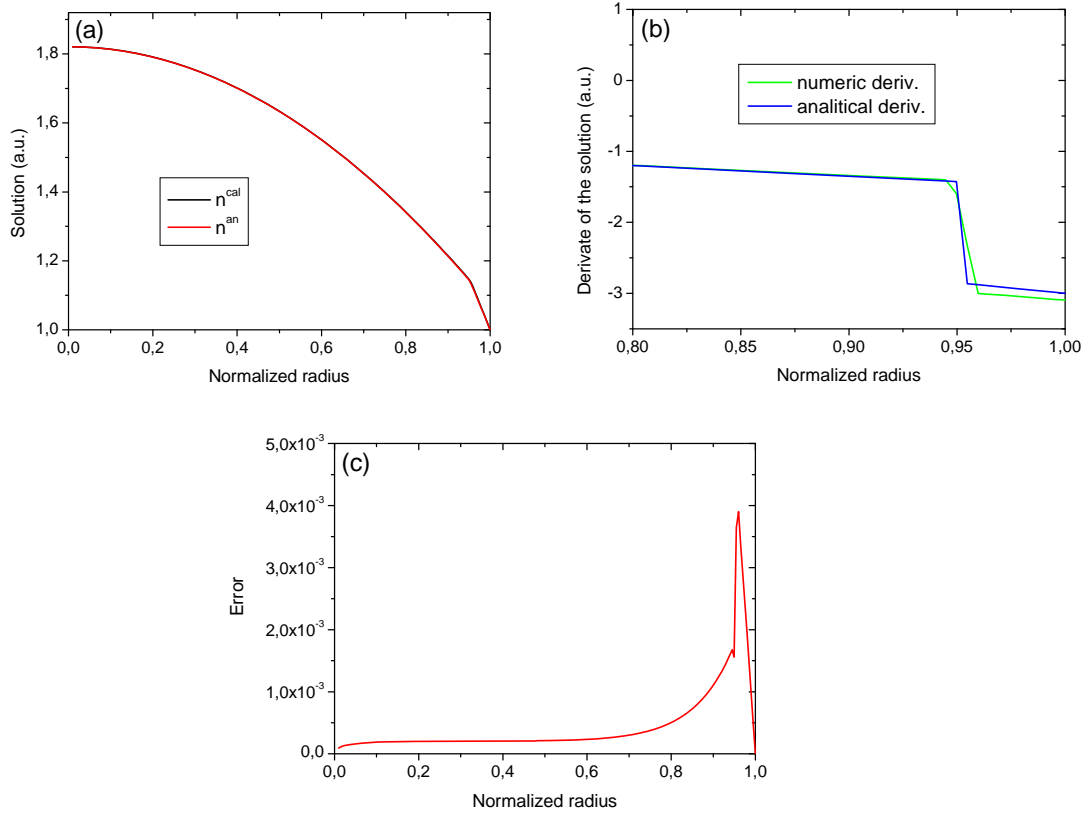
Fig. 24. Analytical and numerical solutions (a), their derivatives (b) and relative error (c) obtained for the first time step $\tau = 10^{-2}$ s, critical radius: $\rho_{cr}\left(\tau = 10^{-2}\,\text{s}\right) = 0.952$.
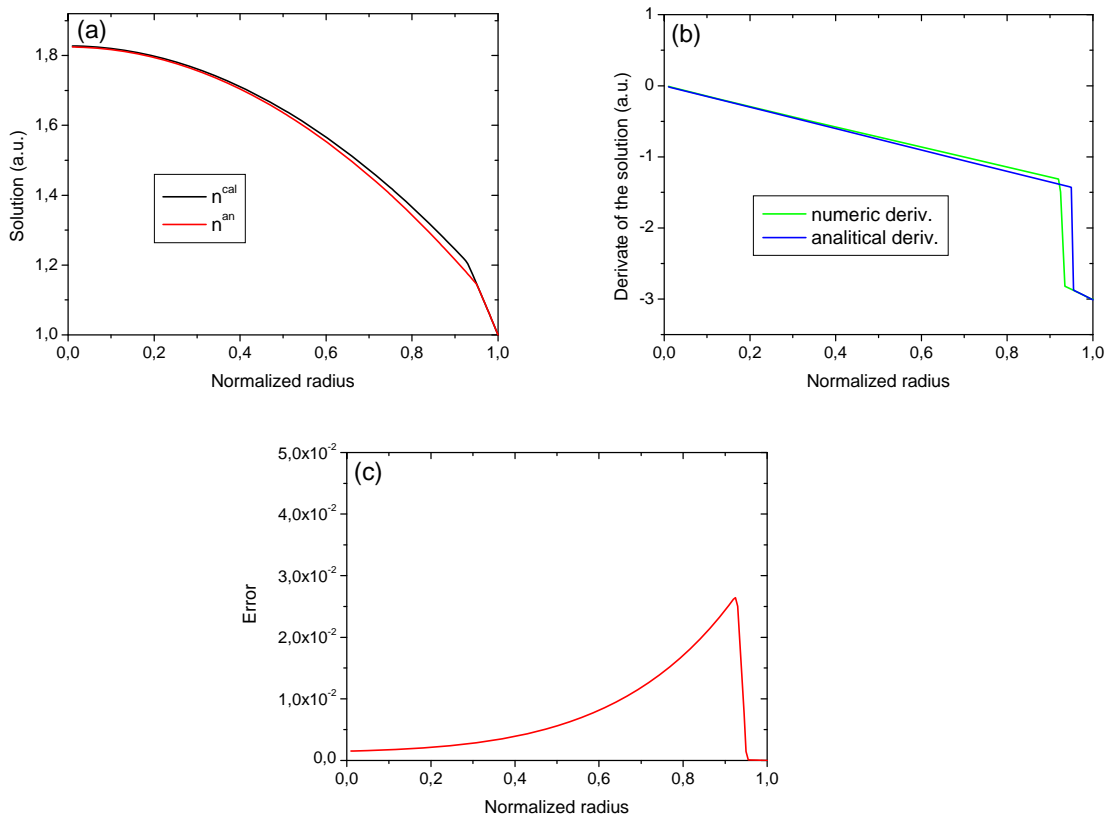

Fig. 25. Analytical and numerical solutions (a), their derivatives (b) and relative error (c) obtained for the tenth time step $\tau = 10^{-1}$ s, where critical radius: $\rho_{cr}\left(\tau = 10^{-1}\,\text{s}\right) = 0.949$.
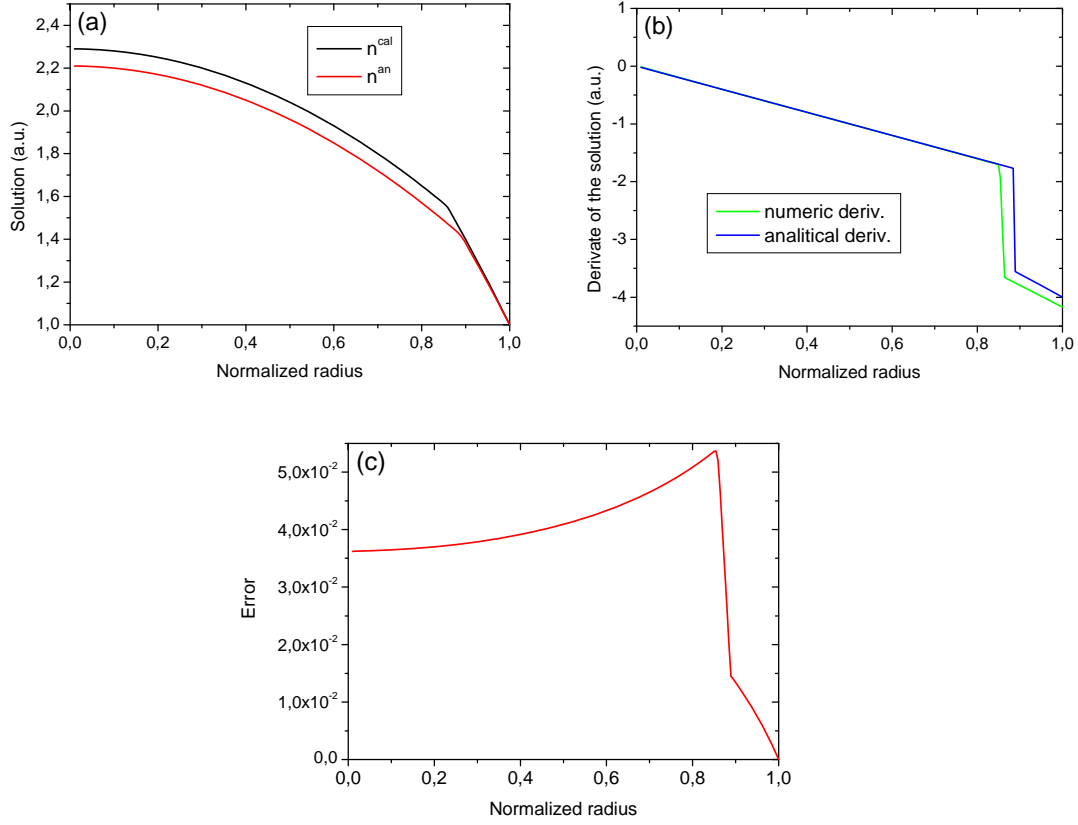
Fig. 26. Analytical and numerical solutions (a), their derivatives (b) and relative error (c) obtained for the last time step $\tau = 10 \, \text{s}$, critical radius: $\rho_{cr}(\tau = 10 \, \text{s}) = 0.886$.

The results presented in Fig. 24, 25, 26 were obtained with the help of solver 7. Numerical solution differ significantly from the analytical one. This difference is rapidly raising close to the critical radius $\rho_{cr}(\tau)$ and decreasing for $\rho > \rho_{cr}(\tau)$. The errors found for solver 3 and solver 7 have tendency to rise for high time step. It is difficult to analyze the full time dependent problem for a solution of the form (10) due to the ambiguity in $\rho_{cr}(\tau)$. Here a correct value of the critical radius was estimated from the derivatives of the analytical solutions. Presumably this is the reason why the errors are so big in this case.

The derivative of the solution with respect to ρ is discontinuous at ρ_{cr}. The ambiguity of critical value comes from the fact that we have two different values of the e-folding length depending on the side from which numerical procedure approaches the discontinuity. According to transport model (7) and flux function (8) the critical radius satisfies the following inequalities:

$$D_i = D_1 \quad \text{for} \quad -\frac{n_i}{D_i(\partial n_i / \partial \rho)} > \frac{L_{cr}}{D_1}$$

and   (18)

$$D_i = D_2 \ll D_1 \quad \text{for} \quad -\frac{n_i}{D_i(\partial n_i / \partial \rho)} < \frac{L_{cr}}{D_1}$$

The right side of inequalities (18) represents the e-folding length divided by diffusion coefficient D_1, below are presented some of the results obtained with the help of this inequality.
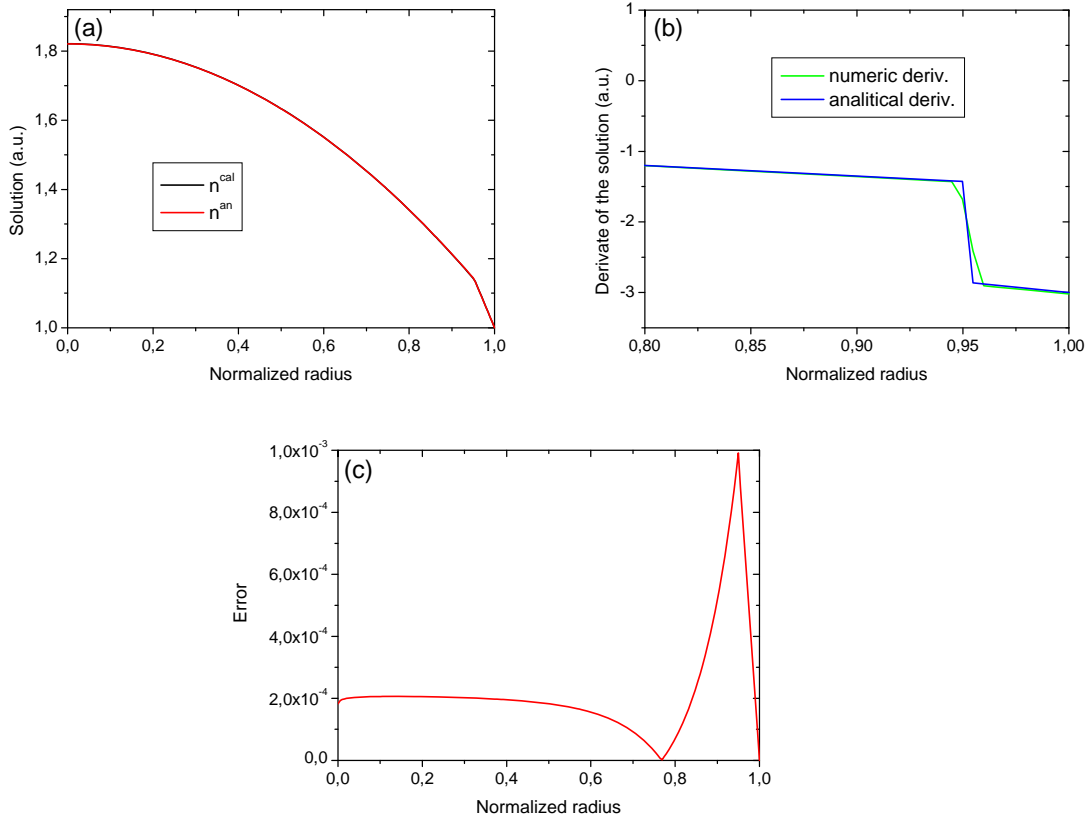

Fig. 27. Analytical and numerical solutions (a), their derivatives (b) and relative error (c) obtained for solver 3 and the first time step $\tau = 10^{-2}$ s, critical radius: $\rho_{cr}\left(\tau = 10^{-2}\,\text{s}\right) = 0.952$.
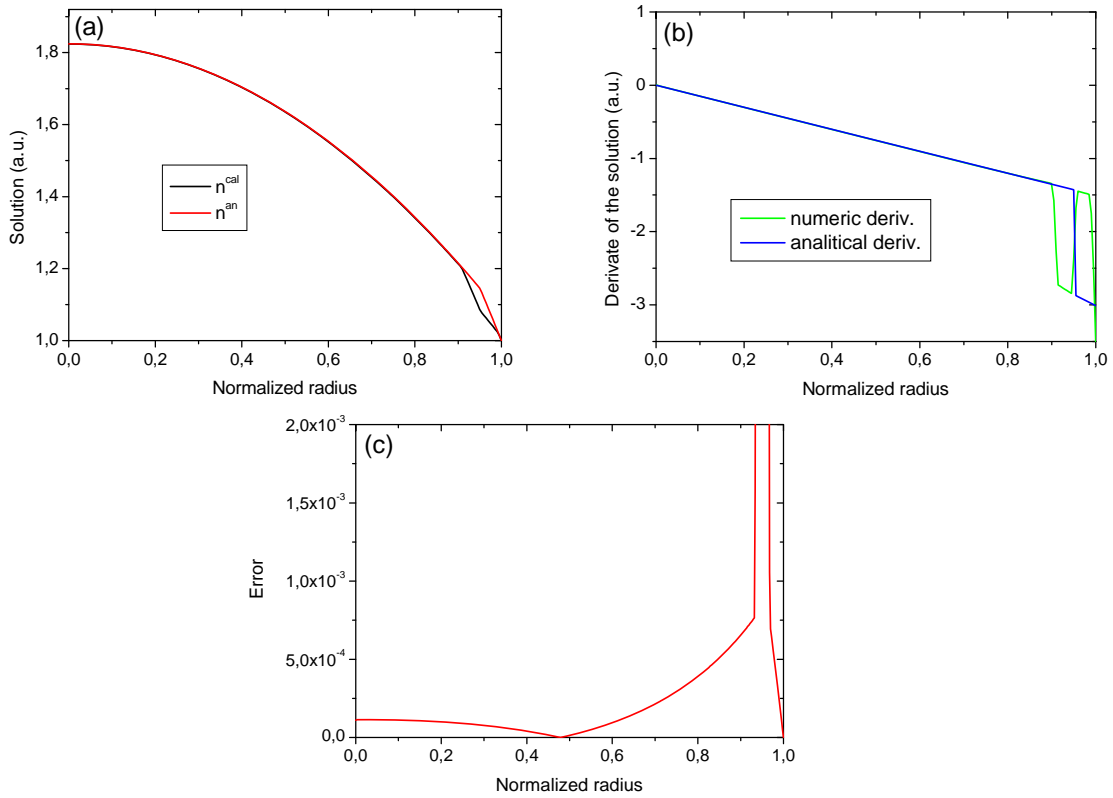
Fig. 28. Analytical and numerical solutions (a), their derivatives (b) and relative error (c) obtained for solver 3 and the tenth time step $\tau = 10^{-1}$ s, critical radius: $\rho_{cr}(\tau = 10^{-1}\text{s}) = 0.949$.
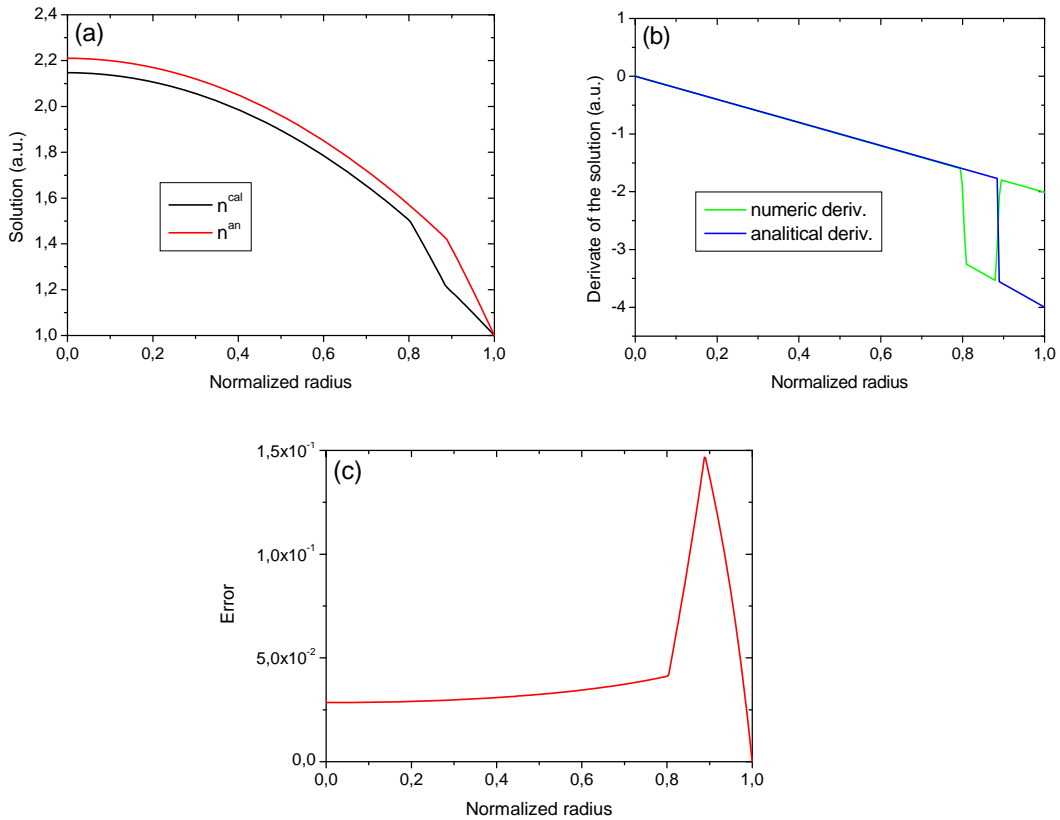

Fig. 29. Analytical and numerical solutions (a), their derivatives (b) and relative error (c) obtained for solver 3 and the last time step $\tau = 10$ s, critical radius: $\rho_{cr}(\tau = 10\,\text{s}) = 0.886$.
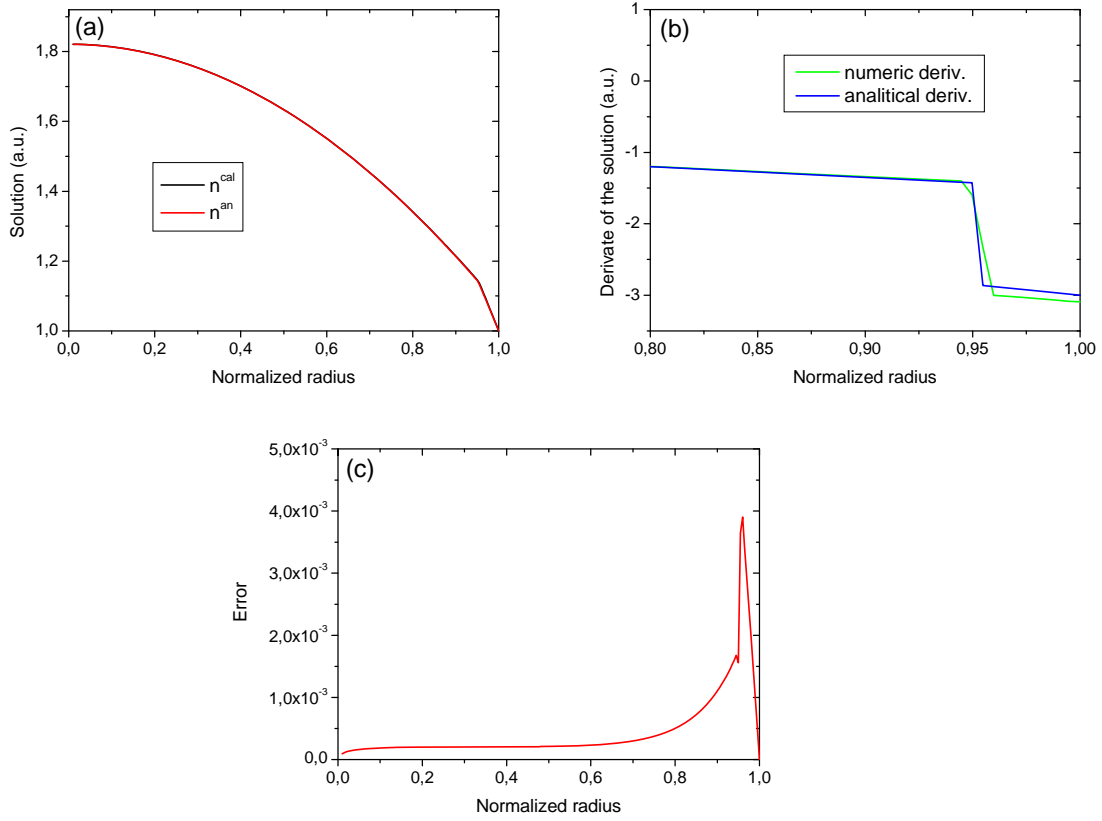
Fig. 30. Analytical and numerical solutions (a), their derivatives (b) and relative error (c) obtained for solver 7 and the first time step $\tau = 10^{-2}$ s, critical radius: $\rho_{cr}(\tau = 10^{-2}\,\text{s}) = 0.952$.
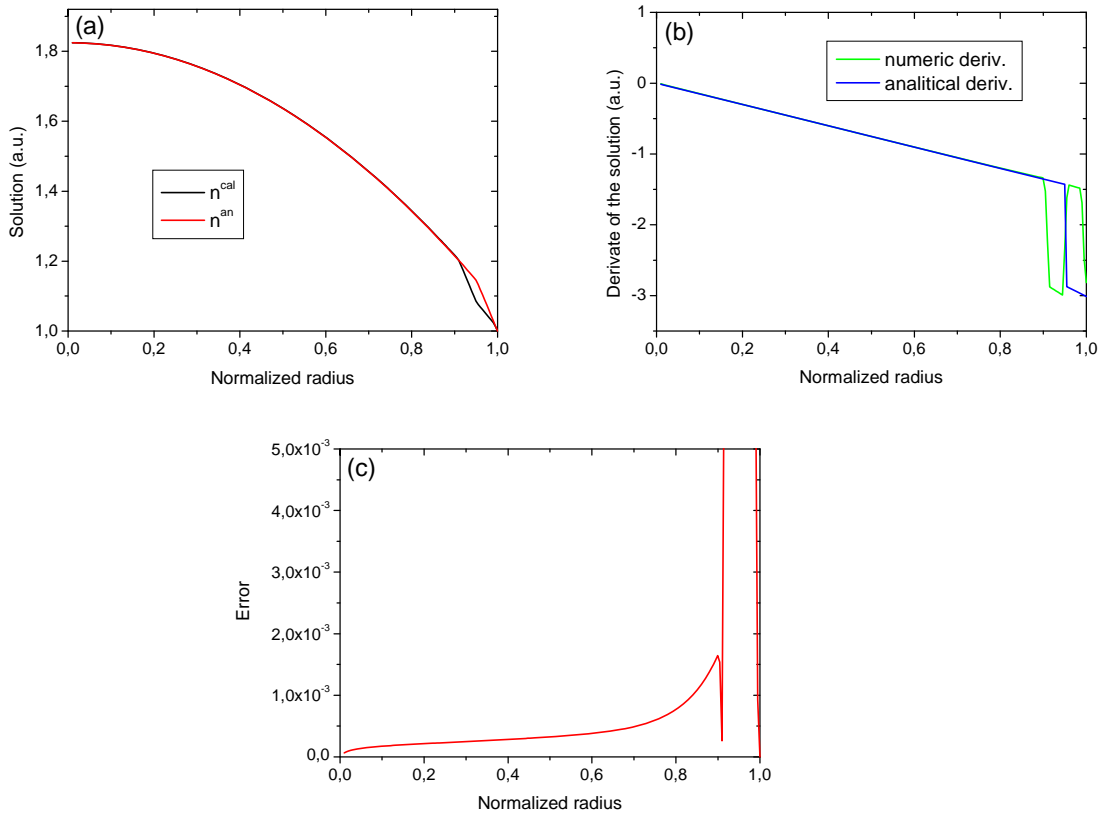

Fig. 31. Analytical and numerical solutions (a), their derivatives (b) and relative error (c) obtained for solver 7 and the tenth time step $\tau = 10^{-1}$ s, critical radius: $\rho_{cr}(\tau = 10^{-1}\,\text{s}) = 0.949$.
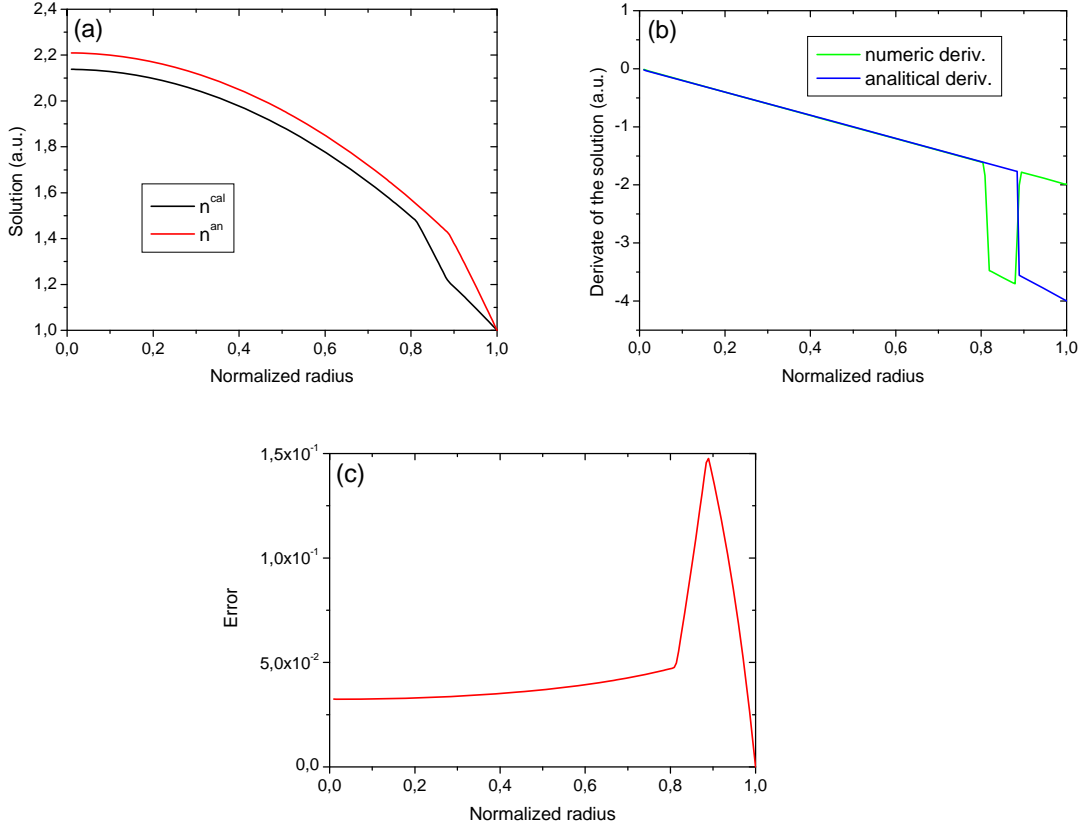
Fig. 32. Analytical and numerical solutions (a), their derivatives (b) and relative error (c) obtained for solver 7 and the last time step $\tau = 10\,\mathrm{s}$, critical radius: $\rho_{cr}(\tau = 10\,\mathrm{s}) = 0.886$.

For this stiff transport formulation (inequality (18)), the results presented in Fig. 27 to Fig. 32 show higher differences between numerical and analytical solutions than in previous cases (Fig. 21 to Fig. 26). This is very well visible if we compare the derivatives of these solutions. When the numerical solver approached to ρ_{cr} then the diffusion coefficient changed from $D_1 = 1$ to $D_2 = 0.5$ and then again returned to the D_1 value. This last change happened exactly in the point where the critical radius calculating from analytic solution is located. The numerical tests demonstrate here that for the time dependent source solvers 3 and 7 can not reproduce the analytical solution with discontinuous derivative but it is important to say that no solutions were obtained for solvers 1 and 2.

6.4. Smooth diffusion function

Stiff transport model can be replaced by a more realistic physical models, where the diffusion coefficient takes a smooth function form. Many models of such functions where $D_1 \gg D_2$ exist in literature, for example [17]:

$$D_i = D_2 + \frac{D_1}{1 + (u'/u'_{cr})^m}, \qquad \text{where } u' = \partial n / \partial \rho. \tag{19}$$

The diffusion coefficient is dependent on the derivative $u'_{cr} = \partial n' / \partial \rho$ and the m parameter, specifying a particular model. For the test needs a simple radially constant source was taken:

$Q = S$ for this type of source the analytic flux $f = S\rho/2$, where $S = 10$, and the diffusion coefficients: $D_2 = 0.1$, $D_1 = 1$. Equation (6) was solved with the help of solver 3 and boundary condition type 1. Numerical computation was provided for the time step $\tau = 10^{-2}$ s and for different sets of the radial points number N. Presented results were obtained for the derivative $u'_c = 4$ which was assumed arbitrary. The analytical solution was obtained with the help of equation (6), which for steady state solution $\partial(\rho n_i)/\partial t = 0$ takes the following form:

$$\left[D_2 + \frac{D_1}{1 + (u'/u'_{cr})^m} \right] u' = -\frac{1}{\rho} \int_0^{\rho} \rho Q d\rho . \tag{20}$$

The solution of equation (20) is represented by derivatives: $u' = \partial n/\partial \rho$. By solving the integral $n = \int_0^{\rho} u' d\rho$ we can find the concentration or the temperature profile. Some of the results obtained for different m are presented below, where the flux is defined according to equation (8).

Fig. 33. Numerical solutions (a), their derivatives (b), diffusion coefficient (c) and flux (d) obtained for solver 3 and $m = 2$, critical radius $\rho_{cr} = 0.48$.
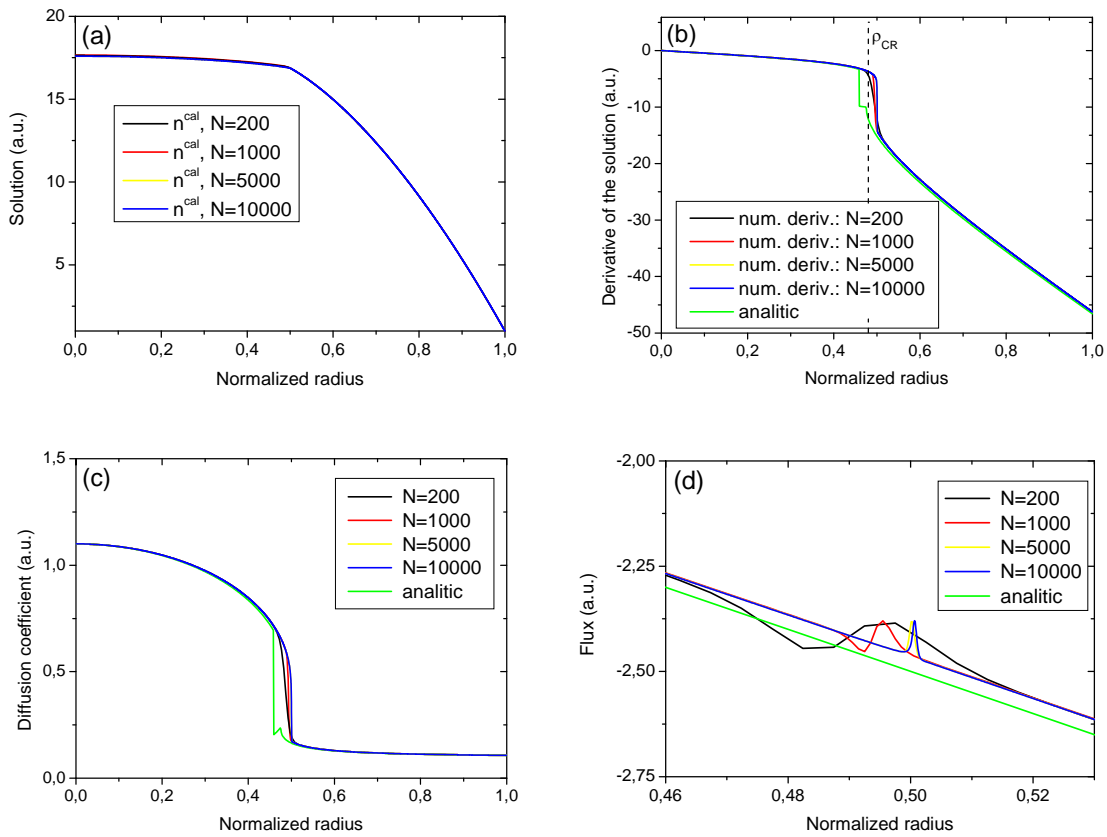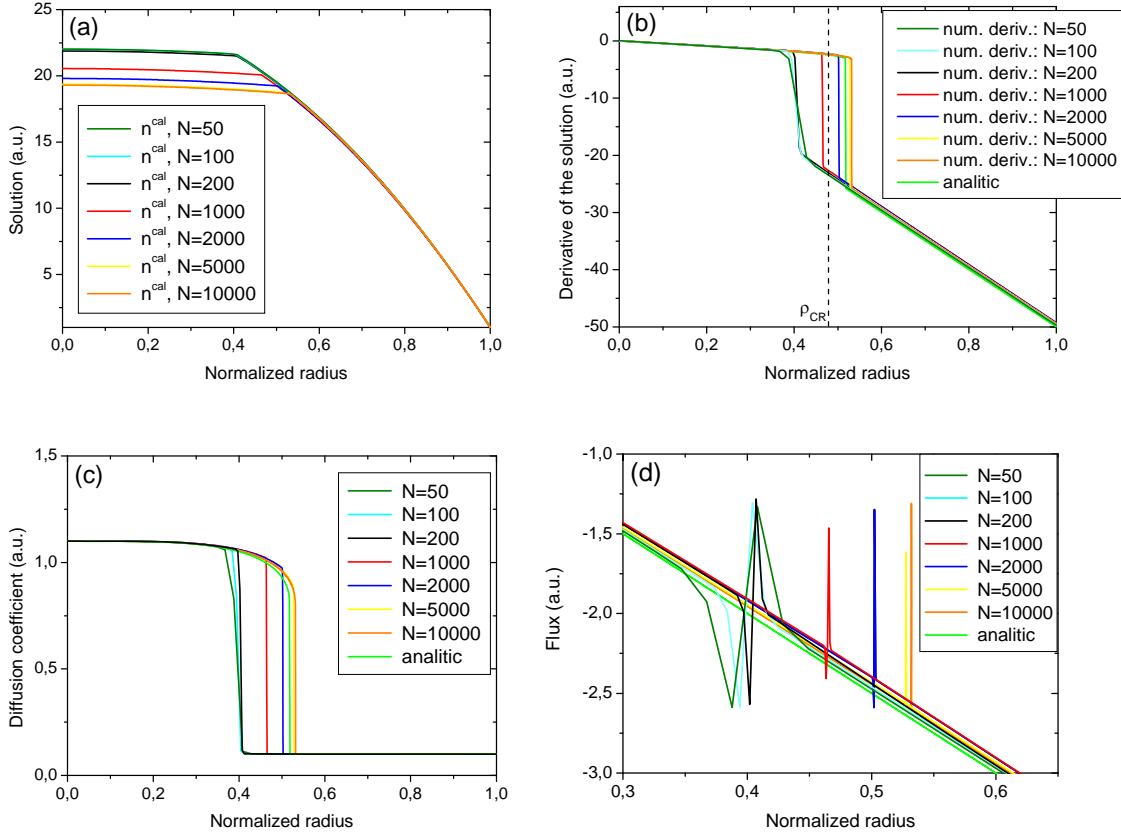
Fig. 34. Numerical solutions (a), their derivatives (b), diffusion coefficient (c) and flux (d) obtained for solver 3 and $m = 4$, critical radius $\rho_{cr} = 0.48$.

The numerical results obtained for $m = 2$ and different sets of the radial points N (Fig. 33) are slightly different from the analytic solution. This difference is very well visible especially in the area where the Internal Transport Barrier (ITB) seems to appear ($\rho_{cr} = 0.48$). The numeric derivatives of the solutions do not fit analytic ones in the area close to ρ_{cr} (Fig. 33b). Numeric fluxes (Fig. 33d) for bigger N are shifted into higher radius value. For higher power $m = 4$ (Fig. 34) numerical solutions become more sensitive to the radial points number N. In this case numerical flux function maxima (Fig. 34d) have more spike shape and are more shifted to the right than it was observed in the previous case. For both presented cases it is possible to find such a number N of the radial points which reproduces most accurately the analytic solution. Numerical calculations were also provided with the help of solver 7 but in this case no solutions were obtained.

6.5. GLF23 diffusion model

For further tests, GLF23 model [18, 19] was used. The diffusion coefficient is defined as $D_i = D_2 + D_{an}$ where:

$$D_{an} = \begin{cases} D_1 (u' - u'_{cr}) / u', & \text{if} \quad u' > u'_{cr} > 0 \\ 0, & \text{if} \quad u' < u'_{cr} \end{cases} \tag{21}$$

The diffusion coefficient, where $D_1 \gg D_2$ and $u' = \partial n / \partial \rho$, is dependent on the critical derivative $u'_{cr} = \partial n' / \partial \rho$ specifying a particular model. The GLF23 model is characterized by very narrow oscillations of numerical solution presented even for a very small time step (Fig. 35). They can be removed by decreasing time step (Fig. 36), but in this case computations become more time consuming. This problem can be avoided by using one of the methods further described in literature [18, 19]. First method base on adding additional diffusion on the l.h.s and subtraction source on the r.h.s of equation (6). The additional source has to be taken for the previous time step. In this way equation (6) turns into following form:

$$\frac{\partial(\rho n_i)}{\partial t} - \frac{1}{\rho}\frac{\partial}{\partial\rho}\left(\rho(D_i + D_s)\frac{\partial n_i}{\partial\rho}\right) = S - \frac{1}{\rho}\frac{\partial}{\partial\rho}\left(\rho D_s \frac{\partial n_i}{\partial\rho}\right)\Bigg|_{(-1)} \tag{22}$$

For the test needs a simple radially constant source was taken: $Q = S$, the analytic flux $f = S\rho/2$, where $S = 10$, and the diffusion coefficients: $D_2 = 0.1$, $D_1 = 1$, $D_S = 10$. The critical derivative was assumed arbitrary: $u'_{cr} = 4$. For this set of parameters $\rho_{cr} = 0.88$.
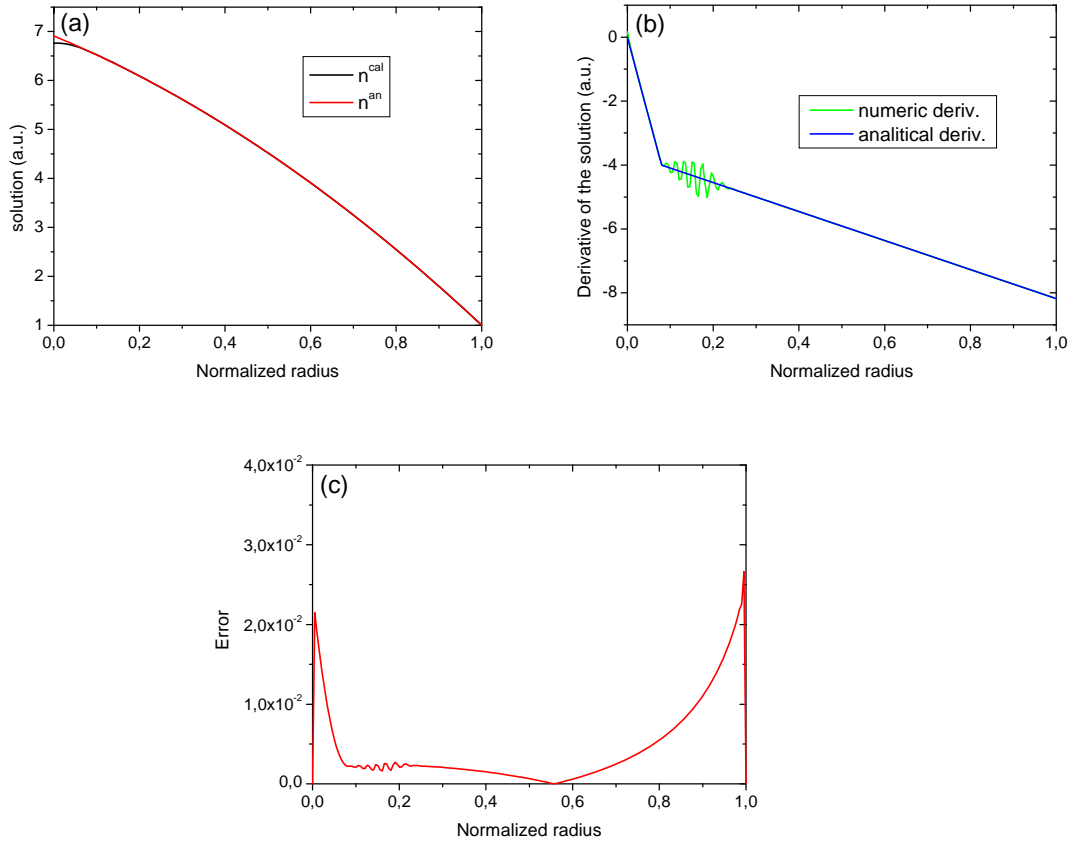

Fig. 35. Numerical solutions (a), their derivatives (b) and relative error (c) obtained for $N = 200$ radial points and $\tau = 10^{-4}$ s.
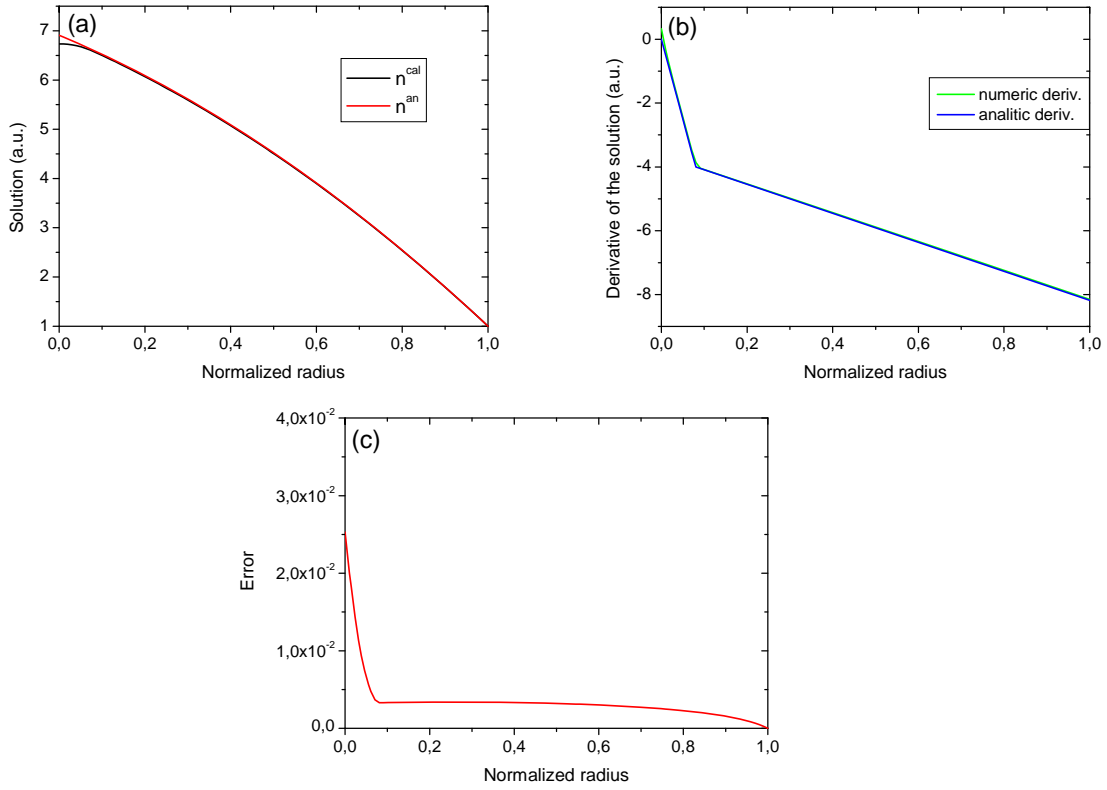
Fig. 36. Numerical solutions (a), their derivatives (b) and relative error (c) obtained for $N = 100$ radial points, $\tau = 10^{-5}$ s.
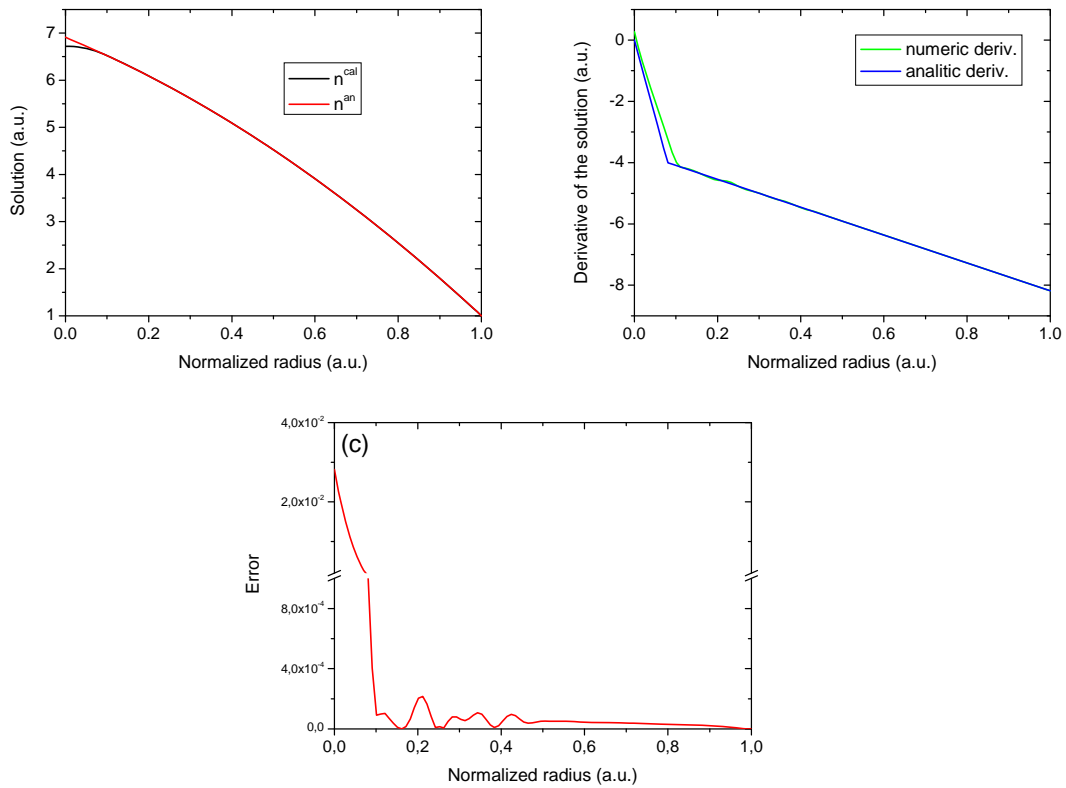

Fig. 37. Numerical solutions (a), their derivatives (b) and relative error (c) obtained for $N = 100$ radial points, $\tau = 10^{-2}$ s and after adding additional diffusion $D_S = 10$.

In Fig. 35 numerical solutions obtained for equation (6) are presented, here numerical oscillations are presented even for a very small time step $\tau = 10^{-4}$ s. They were removed by adding additional diffusion D_s (Fig. 37) and solving equation (22). Oscillations remove method presented by equation (22) allow to increasing time step (Fig. 37) and decreasing computation time. Presented numeric solutions are charged by smaller error which started to raise in response of increasing time step. Equation (22) was solved with the help of solver 3 which was adjusted for the test needs by including an additional source inside solver procedure, no solution was found for solver 7.

7. Conclusions

The existence of the transport barriers is very important for improvement of plasma performance. For the ETS testing needs this phenomen was simplified to a model in which the constant diffusion coefficient changes abruptly when the e–folding length approaches to the critical value. Five solvers are currently implemented in the ETS: solver 1 ("standard" RITM), solver 2 ("integral" RITM), solver 3 ("PROGONKA" block Thomas) and solver 6 and 7. A series of test cases, aimed to quantify solutions of different kinds of solvers, has been carried out. The presented group deals with a reduced set of transport equations in a simplified cylindrical geometry where the constant transport coefficient changes abruptly when the scale length reduces below the critical value. These strongly non-linear stiff transport modules are believed to describe tokamak transport driven by plasma micro-turbulences. The code was run using present framework. Four solvers, 1, 2, 3 and 7, have been tested separately at the presence of three different boundary conditions: type 1 (value), type 3 (scale length) and type 5 (generic). The calculations have been done for a different time steps and iterations numbers. The steady state solutions were compared with the analytical ones. Provided tests reveal that solver 3 deal with this problem with smallest errors then other solvers do, but for the time dependent problem solvers 3 and 7 are not able to reproduce analytic solution.

This solvers "malfunction" can be explained by the fact that in the case where the transport coefficient changes strongly through the volume, a large numerical error arises. In the case when the barrier position is not known in advance, as it is in the time dependent problem, a large number of iterations M is needed to achieve convergence with the analytic solution. A further verification of the ETS will include about twenty various tests to assess the numerical properties and to find the actual limits of the solver applicability. In addition to the numerical reliability, a physical credibility of each solver will be tested.

References

[1] J. D. Lawson, *Some Criteria for a Power Producing Thermonuclear Reactor*, Proc. Phys. Soc. **B 70** (1957), No. 445, p. 6

[2] J. Wesson, *Tokamaks*, 2nd ed., Oxford, Calderon Press, (1997), p. 11

[3] L. Spitzer *U. S. Atomic Energy Commission Report* (1951), No. NYO-993 (PM-S-1)

[4] B. Weyssow, *Neoclassical Transport Properties of Tokamak Plasmas*, 9th Carolus Magnus Summer School on Plasma and Fusion Energy Physics (Herbeumount-sur-Semois, Belgium) **57D** (2009), No. 2T, p. 330-337

[5] A. G. Peeters, *The Bootstrap Current and its Consequences*, Plasma Phys. Control. Fusion **42** (2000), p. 231-242

[6] Available: http://www.efda.org/ [Online]

[7] F. Wagner *et al.* ,*Regime of Improved Confinement and High Beta in Neutral-Beam-Heated Divertor Discharges of the ASDEX Tokamak*, Phys. Rev. Lett. **49** (1982), p. 1408-1412

[8] R. J. Taylor *et al.*, *H-Mode Behavior Induced by Cross-Field Currents in a Tokamak*, Phys. Rev. Lett. **63** (1989), p. 2365-2368

[9] *ITER Physics Basis*, Nucl. Fusion **39** (1999), No. 12**,** Part 1**,** p. 2137-2173

[10] D. P. Coster *et al.*, *The European Transport Solver*, IEEE Transactions on Plasma Science **38** (2010), p. 2085-2092

[11] F. L. Hinton *et al.*, *Theory of Plasma Transport in Toroidal Confinement Systems*, Rev. of Modern Physics **48** (1976), No. 2, Part 1, p. 239-308

[12] D. Kalupin *et al.*, 35th EPS Conference on Plasma Physics (Hersonissos, Grece) **32**D (2008), p. 5027-5030

[13] F. Imbeaux *et al.*, 35th EPS Conference on Plasma Physics (Hersonissos, Grece) **32**D (2008), p. 2112-2115

[14] D. P. Coster *et al.*, 21th International Conference on Numerical Simulation of Plasma (Lisbon, Portugal) (2009)

[15] G. V. Pereverzev *et al.*,13th European Fusion Theory Conference (Riga, Latvia) (2009)

[16] M. Z. Tokar *et al.*, *Numerical Solution of Transport Equations for Plasmas With Transport Barriers*, Computer Physics Communications **175** (2006), p. 30-35

[17] W. Horton *et al.*, *Transport Barrier Dynamics*, Phys. Plasmas 7 (2000), p. 4534-4547

[18] S. C. Jardin *et al.*, *On 1D Diffusion Problem With a Gradient-Dependent Diffusion Coefficient*, Journal of Computational Physics **227** (2008), p. 8769-8775

[19] G. V. Pereverzev *et al.*, *Stable Numeric Schame for Diffusion Equation With a Stiff Transport*, Computer Physics Communications **179** (2008), p. 579-585